Congyuan Li[1], Ning Zhang[1] and Yongwei Wang[2]

[1] School of Atmospheric Sciences, Nanjing University, Nanjing, China.

[2] Nanjing University of Information Science and Technology,School of Atmospheric Physics, Nanjing, 210044, China

Corresponding author: Ning Zhang (ningzhang@nju.edu.cn)

Key Points:

- The Community Land Model Urban (CLMU) was developed by incorporating the local climate zones (LCZs) framework
- The intra-urban variability of urban heat islands (UHIs) and urban thermal comfort modulated by background climate in the 2013 heatwave episode were explored
- The dominant factors of surface UHIs vary with intra-urban heterogeneity and are also regulated by heat wave intensity and local climate

Abstract

The urban expansion-induced heat can deteriorate heat stress for urban dwellers, especially during heat waves. With a focus on the intra-urban variability of urban heat islands (UHIs) and thermal comfort, the urban parameterization within the Community Land Model version 5 (CLM5) was modified to incorporate the local climate zones (LCZs) framework (i.e., CLM5-LCZs) to simulate the urban climate during a heat wave (HW) event in the summer of 2013 in East China. The simulations were validated by observation data from a flux tower measurement site, conventional stations and automatic meteorological stations, which exhibits a reasonable agreement. The aim of this work was to investigate: 1) the variability of temperature and heat stress in relation to each urban LCZ, 2) the influence of intra-urban inhomogeneity on attributing factors of SUHII, 3) the response of canopy urban heat island intensity (CUHII) and surface urban heat island intensity (SUHII), urban thermal comfort and controlling factors of SUHII to HW. The results show that daytime and nighttime CUHII were highest in the Compact Low Rise (LCZ3) and the Compact High Rise (LCZ1) areas, respectively. SUHII separately peaked in the Large Low Rise (LCZ8) and the Compact High Rise (LCZ1) areas during daytime and nighttime. Contrasts of CUHII and SUHII between urban classes could exceed 1.7 °C and 5.4°C which varied with background climate and HW episode. Urban dwellers were exposed to the most serious heat stress in LCZ3 and LCZ1 areas over the north subtropical climate zone. The intra-urban heterogeneity resulted in the changes in dominant factors controlling SUHII that were modulated by local climate and HW intensity. Moreover, UHIs and thermal comfort were obviously affected by the occurrence of HW events such as the changes in CUHII for the Lightweight Low Rise (LCZ7, 1.0°C) and SUHII for LCZ8 (3.8°C).

Plain Language Summary

The Community Land Model Urban (CLMU) is the urban parameterization within the Community Land Model version 5 (CLM5) to simulate urban climate and human thermal comfort. The local climate zones (LCZs) framework have been utilized to facilitate communications and studies of urban climate knowledge, which was applied to update the CLMU by substituting the current urban density class representation in the model in this study. The modified model was evaluated by comparing its results with observations to demonstrate its credibility. This work aimed to investigate: 1) the intra-urban variability of urban heat islands (UHIs) and heat stress during the heat wave episode, 2) the impact of urban features on UHIs, 3) the response of UHIs, thermal comfort and controlling factors of UHIs to the occurrence of heat waves. It is useful to investigate the features, causes and controls of UHIs as well as the combined effects of heat waves and UHIs for this improved model. The results indicate that temperature behaviors and thermal comfort levels vary with urban form and materials. This intra-urban heterogeneity significantly affects quantitative contributions to surface UHIs from the urban-rural contrast of various biogeophysical properties, which are regulated by local background climate and heat wave intensity.

1 Introduction

Urban heat islands (UHIs), manifested as higher temperatures in urban areas than in their surroundings, are a remarkably growing concern in recent decades on account of their implications for climate change and population growth (Arnfield, 2003; Grimm et al., 2008; Hsu et al., 2021; Manoli et al., 2019; Yong Sun et al., 2021; L. Zhao et al., 2014; Zhao et al., 2021; Zhong et al., 2021). Urban heat island intensity (UHII) generally could be interpreted as canopy UHI intensity (CUHII) or surface UHI intensity (SUHII), defined as the difference in surface air temperature or surface skin temperature between urban and rural areas. The causes of UHIs relate to the urban-rural contrast of surface structure and cover, such as greater absorption of solar radiation due to lower albedo and multiple reflections and radiation trapping, lower rates of evaporative cooling due to less vegetation cover in cities (S. Grimmond, 2007; D. Li et al., 2019; Oke, 1982). As illustrated by Hamdi et al. (2020) and Masson et al. (2020), there are three main factors contributing to urban-enhanced warming: 1) urban geometry, 2) anthropogenic heat, and 3) thermal properties. Local background climate (L. Zhao et al., 2014) and aerosols (Cao et al., 2016; Han et al., 2020) can also modulate UHI intensity. UHIs are a form of heat pollution for urban dwellers and deteriorate urban environment and human health (Bai et al., 2018; Sen & Khazanovich, 2021). Moreover, UHIs may interact with extremely high-temperature events such as heat waves that further exacerbate heat stress in cities (D. Li & Bou-Zeid, 2013; Liao et al., 2018; T. Sun et al., 2017; Zhao et al., 2018).

Urban areas are becoming increasingly vulnerable to heat wave episodes. The intensity, frequency, and duration of heat waves (HW) have shown an increasing trend across China in recent decades (Ao et al., 2019; Ying Sun et al., 2014).

Given climate change and urban development, the future likelihood of HW is projected to further raise (Ying Sun et al., 2014; Zheng et al., 2021). Hence it is essential to quantify the UHIs-HW interaction and the impacts of synergies between UHIs and HW on human thermal comfort. Many diagnostic and prognostic methods, such as Heat Index (HI) (Rothfusz, 1990) or the Simplified Wet-Bulb Globe Temperature (SWBGT) (Willett & Sherwood, 2012), has been designed as heat stress metrics to account for comfort level. These metrics are derived from combinations of air temperature, humidity, wind speed, and so on. Buzan et al. (2015) implemented a module of heat stress indices (four moist thermodynamic quantities and nine heat stress metrics) in the Community Land Model (CLM) (Lawrence et al., 2019) that could be utilized to assess the urban-rural contrast of human thermal comfort.

Urban parameterization used to describe urban surface-atmospheric exchanges of heat, momentum and water can be classified: 1) the slab or bulk model, 2) single-layer urban canopy model, 3) multi-layer urban canopy model (C. S. B. Grimmond et al., 2011; C. S. B. Grimmond et al., 2010; Masson, 2006). According to Best and Grimmond (2015) and Daniel et al. (2019), it is sufficient for a single-layer urban canopy model to simulate UHIs at a regional scale. Given urbanization as an important aspect of anthropogenic change in climate science, urban parameterizations are being incorporated into regional and global climate models (F. Chen et al., 2011; Daniel et al., 2019; Hertwig et al., 2021; Oleson, Bonan, Feddema, & Vertenstein, 2008; Oleson, Bonan, Feddema, Vertenstein, et al., 2008), although global modeling groups participating in the Coupled Model Intercomparison Project Phase 6 (CMIP6) (Eyring et al., 2016) mostly lack these urban schemes (Zhao et al., 2021). Oleson et al. (2011) implemented a parameterization for urban areas (i.e., the Community Land Model Urban (CLMU)) within the CLM of the Community Earth System Model (CESM) (Hurrell et al., 2013) to simulate UHIs characteristics.

The state-of-the-art regional and global climate models that have urban schemes, such as the Weather Research and Forecasting (WRF) model (Skamarock & Klemp, 2008) and the most recent version of CLM (CLM5-CESM2), universally simulate three urban density classes (i.e., tall building district (TBD), high and medium density(HD, MD)) within each model grid cell. However, the current urban density class representation may not capture the variations in urban microclimates, and it has little climatological relevance. Stewart and Oke (2012) developed a new climate-based 'Local Climate Zones' (LCZs) classification system to facilitate the communications and studies of UHIs. Based on the specific combination of surface cover, structure and fabric, and human activity, it comprises 10 urban built types. Recent studies demonstrated that each LCZ portrays a unique thermal behavior and comfort under similar atmospheric and surface relief conditions (Bechtel, Demuzere, et al., 2019; Kotharkar et al., 2021; J. Yang et al., 2021; X. Yang et al., 2018), and highlighted it would likely be beneficial to incorporate LCZ classification into the model (Alexander et al., 2015; Mughal et al., 2019; Oleson & Feddema, 2020; Stewart et al., 2014).

The inter-LCZ temperature and humidity variability (Núñez-Peiró et al., 2021; X. Yang et al., 2020; X. Yang et al., 2018) imply that human thermal comfort and building energy use are heterogeneous within cities. Especially during heat wave episodes, the individual local site may face very severe heat stress and energy demand. It could guide research on the causes and controls of UHIs to utilize LCZ classification in numerical models (Mughal et al., 2020; Stewart & Oke, 2012). HW-induced changes in CUHI and SUHI variations have been investigated (Liao et al., 2021; Miao et al., 2022; Shi et al., 2021; J. Wang et al., 2021), however, the response differences of UHIs in relation to urban LCZs to HW across background climates remain unclear. It is necessary to identify maximum 'extremely hot' condition and 'no heat risk' condition at the LCZs level during the HW episodes.

Previous studies have analyzed the controlling factors of spatial variations of SUHII (C. Li & Zhang, 2021; D. Li et al., 2019; L. Zhao et al., 2014) across different cities or local climate s. Nevertheless, the impact of intra-urban heterogeneity (i.e., various urban features, including morphology, fabric, etc.) on SUHII remains largely unclear, and the role of HW intensity in quantitative contributions from intra-urban variations needs to be further investigated.

The present study employed the modified CLM5-CESM to simulate energy and water exchanges between urban areas and the atmosphere by substituting the current urban density class representation with the LCZ classification system in urban parameterization (i.e., CLMU-LCZs). The observational data from a flux tower measurement site and automatic meteorological stations were used to evaluate the performance of the CLMU-LCZs by conducting a single-point case and a regional case across Nanjing. Moreover, we conduct a regional simulation in East China with LCZs map and specific parameters in relation to each urban LCZ. In this study, the spatial pattern and diurnal cycle of canopy UHII (CUHII), surface UHII (SUHII) and urban heat stress for each urban LCZ were investigated during a HW period in East China. We also investigated the impacts of the occurrence of HW on UHIs and human comfort by defining HW and non-HW (NHW) days. Furthermore, the intrinsic biophysical mechanism (IBM) method utilized to attribute SUHII variations to several controlling factors was applied to analyze the changes in dominant factors among different urban LCZs, and the impact of HW intensity and local climate on them.

2 Model and Modeling Setup

2.1 Incorporating LCZs framework into the CLM5

In this study, we employ the modified urban parameterization incorporating the LCZ classification system (i.e., CLM5-LCZs) within version 5 of the CLM (Lawrence et al., 2019) as the land component of the CESM version 2 (Danabasoglu et al., 2020). The corresponding modules and codes for geophysical processes, input and output were revised. The CESM has been widely used in climate studies that contributed to the CMIP (Blackport et al., 2021; Eyring et al., 2016; Zhao et al., 2021; Zheng et al., 2021). Moreover, it allows for the

investigations of both global urban climate questions and local urban environment under various climate change scenarios. Recent works utilizing this model to identify the features and causes of UHIs motivate further studies on urban climates and developments for urban schemes (Meier et al., 2021; Oleson & Feddema, 2020).

Land heterogeneity in CLM5 is represented as the subgrid hierarchy, comprising several land units: vegetated, lake, glacier, crop and urban. The urban parameterization is represented by the Community Land Model Urban (CLMU) that divided urban land units into three density classes including TBD, HD and MD for current urban parameterization. As suggested by Oleson and Feddema (2020) and Masson et al. (2020), the transition from density classes to the LCZ classification system in the model may contribute to understanding and exchange of urban climate knowledge. Surface energy budgets and surface temperature are separately calculated at each of five urban canyon facets: roof, sunlit wall, shaded wall, and pervious and impervious roads. Evaporation in pervious surface is characterized with a simplified bulk scheme without explicit representation of urban vegetation. Anthropogenic heat from space heating and air conditioning system is parameterized by a building energy submodel. In contrast, the corresponding variables over the adjacent rural areas are calculated from the weighted average of vegetated, crop, lake and glacier land units. The compositions and area fractions of rural lands were derived from the Moderate Resolution Imaging Spectroradiometer (MODIS) data, and the biogeophysical parameters were extracted from prescribed values in CLM5. The vegetation land unit consists of 15 possible plant functional types (PFTs, e.g., needleleaf evergreen tree), and the crop land unit comprises 64 crop functional types (CFTs, e.g., rainfed temperate corn). Therefore all variables for an urban-rural site pair or urban LCZs-rural pairs could be available.

Table 1. Input parameter values of each urban LCZ for the CLM5-LCZs

	Local Climate Zones (LCZs)								
	1	**2**	**3**	**4**	**5**	**6**	**7**	**8**	**9**
Land Cover									
f_b	0.50	0.50	0.55	0.30	0.30	0.30	0.75	0.40	0.15
f_i	0.45	0.40	0.30	0.35	0.40	0.40	0.10	0.45	0.15
f_p	0.05	0.10	0.15	0.35	0.30	0.30	0.15	0.15	0.70
Morphological									
H	37.5	17.5	6.5	30.0	17.5	6.5	3.0	6.5	6.5
HW	2.5	1.25	1. 25	1.0	0.5	0.5	1.5	0.2	0.15
z_r	0.3	0.3	0.2	0.3	0.25	0.15	0.1	0.12	0.15
z_w	0.3	0.25	0.25	0.2	0.2	0.2	0.1	0.2	0.2
Radiative									
α_r	0.23	0.28	0.25	0.23	0.23	0.23	0.55	0.28	0.23
α_w	0.35	0.30	0.30	0.35	0.35	0.35	0.55	0.35	0.35
α_i	0.14	0.14	0.14	0.14	0.14	0.14	0.18	0.14	0.14

	Local Climate Zones (LCZs)								
α_p	0.22	0.22	0.22	0.22	0.22	0.22	0.22	0.22	0.22
ε_r	0.91	0.91	0.91	0.91	0.91	0.91	0.88	0.91	0.91
ε_w	0.90	0.90	0.90	0.90	0.90	0.90	0.90	0.90	0.90
ε_i	0.91	0.91	0.91	0.91	0.91	0.91	0.88	0.91	0.91
ε_p	0.95	0.95	0.95	0.95	0.95	0.95	0.95	0.95	0.95
Thermal									
λ_r	1.70	1.70	1.09	1.25	1.70	1.09	0.50	1.07	1.09
λ_w	1.27	2.60	1.66	1.45	1.88	1.66	0.18	1.07	1.66
λ_i	0.78	0.78	0.78	0.78	0.78	0.78	0.78	0.78	0.78
c_r	1.32	1.32	1.32	1.80	1.32	1.32	2.00	2.11	1.32
c_w	1.54	1.54	1.54	2.00	1.54	1.54	2.00	2.11	1.54
c_i	1.85	1.85	1.85	1.85	1.85	1.85	1.85	1.85	1.85
$\mathrm{T_{ib,\ max}}$	25.0	25.0	25.0	25.0	25.0	25.0	25.0	25.0	25.0
$\mathrm{T_{ib,\ min}}$	10.0	10.0	10.0	10.0	10.0	10.0	10.0	10.0	10.0

* f_b, f_i and f_p denote urban building plan area fraction, impervious road fraction and pervious road fraction, respectively. H, HW, z_r and z_w denote mean building height (m), mean canyon height-to-width ratio, roof thickness (m) and wall thickness (m), respectively. α_r, α_w, α_i and α_p denote roof albedo, wall albedo, impervious road albedo and pervious road albedo, respectively. ε_r, ε_w, ε_i and ε_p denote roof emissivity, wall emissivity, impervious road emissivity and pervious road emissivity, respectively. λ_r,λ_w and $\lambda_i$denote roof thermal conductivity, wall thermal conductivity and impervious road thermal conductivity (W m^{-1} K^{-1}), respectively. c_r, c_w and c_i denote roof volumetric heat capacity, wall volumetric heat capacity and impervious road volumetric heat capacity (MJ m^{-3} K^{-1}), respectively. $\mathrm{T_{ib,\ max}}$ and $\mathrm{T_{ib,\ min}}$ represent max interior building temperature and min interior building temperature (℃), which could be utilized to estimate the anthropogenic heat flux in cities.

LCZ classification scheme is used in the model to expand urban landunits to better describe inter-urban variability of temperature or humidity regimes and thermal comfort. All urban variables are estimated at each landunit of 10 urban LCZs. In addition to area fractions of each urban LCZ derived from the LCZ map, it is essential to convert urban canopy parameters to be suitable for the representation of each urban LCZ. The present study refers to the LCZ parameter information described in previous studies (Bechtel et al., 2015; Stewart et al., 2014; Zonato et al., 2021). Table 1 shows the morphological, thermal and radiative parameters for urban LCZs adapted to the simulations with the CLM5-LCZs.

2.2 The LCZs Map

The LCZs scheme is a climate-oriented description of the urban landscape based on the controls of surface climates (i.e., surface cover, structure, material, and

human activity) with a horizontal scale of hundreds of meters to several kilometers. It comprises 17 standard LCZs, of which 10 are built-up types (i.e., urban LCZs) and 7 are natural land cover types. The urban LCZs consist of the Compact High Rise (LCZ1), the Compact Mid Rise (LCZ2), the Compact Low Rise (LCZ3), the Open High Rise (LCZ4), the Open Mid Rise (LCZ5), the Open Low Rise (LCZ), the Lightweight Low Rise (LCZ7), the Large Low Rise (LCZ8), the Sparsely Built (LCZ9) and the Heavy Industry (LCZ10). According to Ching et al. (2018) and Bechtel, Alexander, et al. (2019), the LCZs map for East China could be developed using available Landsat images, Google Earth for creating the training areas and the System for Automated Geoscientific Analyses software. The area fractions of each urban LCZ for East China and the city of Nanjing were separately exhibited as Figure 1 and Table 2. For the single-point case with the CLM5-LCZs, the majority of urban landscapes is the LCZ2 within 1.0 km around the observation site in Nanjing. The dominant urban classes vary with different climate zones for the regional case in East China.

Table 2. Area fractions of LCZs types for single-point simulation in Nanjing

	CLM5 – 10 urban LCZs	**Vegetation**							
	1	**2**	**3**	**4**	**5**	**6**	**7**	**8**	**9**	**1**
Area fractions	0.095	0.388	0.051	0.122	0.122	0.02	0	0.003	0	0

2.3 Experimental Design

Table 3. The design of experiments in this study

Cases	Models	Simulation types	Urban land-use	Study area
1	CLM5-U3	single-point	TBD, HD, MD	Nanjing
2	CLM5-LCZs	single-point	LCZs	Nanjing
3	CLM5-LCZs	regional	LCZs	Nanjing
4	CLM5-LCZs	regional	LCZs	East China

Table 3 exhibits the experiments conducted in this study. Case 1, Case 2 and Case 3 were utilized to evaluate the performance of the CLM5-LCZs with observations, whereas Case 1 implemented by default CLM5 (CLM5-U3) and Case 2 implemented by the CLM5-LCZs was forced by meteorological data (i.e., wind, air temperature, atmospheric pressure, specific humidity, precipitation, and downward shortwave radiation) obtained from conventional weather stations (32.03°N, 118.79°E) in Nanjing. Meanwhile, surface energy balance data (net radiation, sensible heat flux, latent heat flux and storage heat flux) obtained from this observation site was used to evaluate the performance of reproducing surface energy balances. These data were measured at a height of 49.5 m (2.5 times of the average height of the buildings) above the ground that was estimated to situate in the inertial sublayer (Zou et al., 2015).

Additionally, for case 3, it was run with atmospheric forcing data derived from the China Meteorological Forcing Dataset (He et al., 2020) which is suitable for studies of land surface processes in China. This simulation was conducted with a spatial resolution of 1km in Nanjing. Through comparing its results with the observational data (including 2-m air temperature and relative humidity) obtained from a measurement network of automatic weather stations, the credibility of the CLM5-LCZs was further validate. This measurement network comprises a total of 36 weather stations, of which 20 stations are situated in building areas and 16 stations are situated in natural land-cover areas.

To investigate spatiotemporal variations of UHIs and its causes, Case 4 was conducted with a spatial resolution of 0.1° in East China using the CLM5-LCZs (Figure 1). It was forced by atmospheric data obtained from the China Meteorological Forcing Dataset. East China, a region along the central-eastern coastline of China (21°N - 41°N, 106 °E - 124°E) , comprises China's three largest urban agglomerations, the Beijing-Tianjin-Hebei agglomeration, the Yangtze River Delta agglomeration, and the Pearl River Delta agglomeration. It has a high city density and urbanization level. The area is located in five Köppen–Geiger climate zones, including the south subtropical (SS), mid subtropical (MS), north subtropical (NS), warm temperate (WT), mid temperate (MT) climate zones, determined by the accumulated background climate (Figure 1).

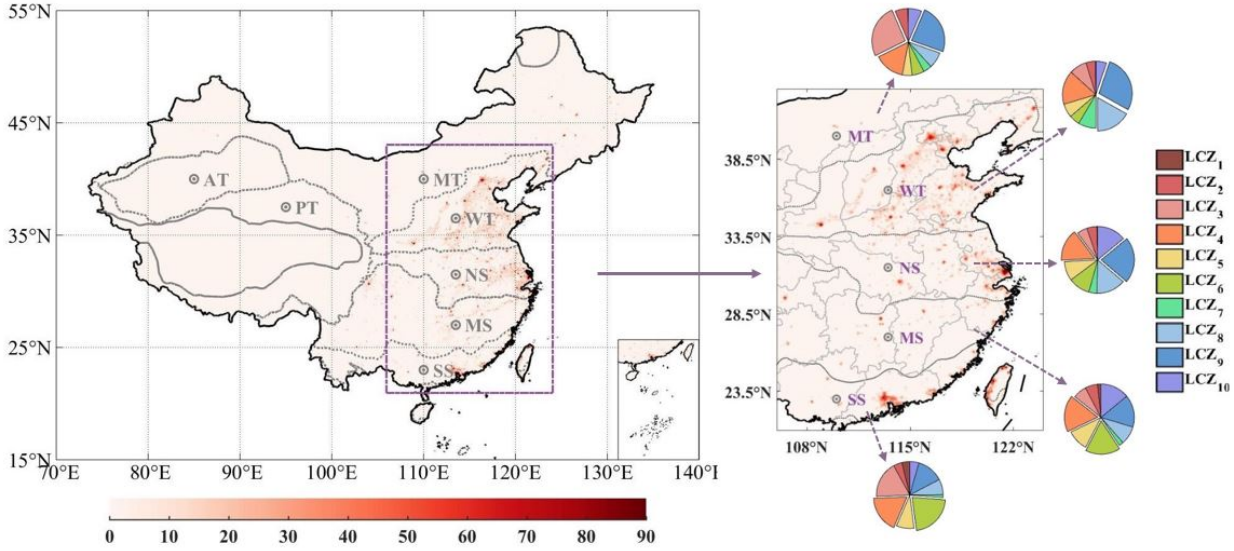

Figure 1. Spatial distribution of total urban area fractions composed of 10 urban LCZs. The highlighted purple box is the simulation domain for the regional case in this study. The SS, MS, NS, WT, MT, AT, and PT denote several Köppen–Geiger climate zones, including the south subtropical, mid subtropical, north subtropical, warm temperate, mid temperate, arid temperate, and plateau temperate climate zones. The pie charts on the right are percentages of each

urban LCZ in cities across the SS, MS, NS, WT, MT climate zones.

Specifically, during 2013, China experienced the hottest summer on record (Ying Sun et al., 2014; Xia et al., 2016), therefore simulations were conducted in this year. The observed daily maximum temperatures almost exceeded 35 °C that could intensify UHI intensity and exacerbate urban heat stress (Y. Chen & Zhang, 2018; X. Wang et al., 2020). In view of this, we analyzed intra-urban variability of UHIs and its controlling factors during the period from 1 July to 31 August in 2013.

3 Model Evaluation

3.1 Evaluation of the CLMU-LCZs

Table 4. Area fractions of default land types for single-point simulation (CLM5-U3) in Nanjing

Land Cover	**CLM5 – 3 urban density classes**	**Vegetation**		
	TBD	HD	MD	
Area fractions	0.095	0.617	0.121	0.167

The modified urban parameterization (i.e., CLMU-LCZs) is the module to describe the urban-atmosphere interaction as one of the important components of land processes (i.e., CLM5-LCZs). Its performance was evaluated with observed flux data ($Rn+Q_{ah}=H+LE+Q_s$), and contrasting it with the performance of the original model (i.e., CLM5-U3, which comprises three urban density classes: TBD, HD and MD). The model was run uncoupled as the single-point case and was forced by atmospheric variables from tower observations in Nanjing during the HW period in 2013. Here, it consists of two single-point simulations, one of which is the case using the CLM5-LCZs and LCZs map, and the other is the case using the CLM5-U3 and default urban land covers (Table 4).

In general, the CLM5-LCZs did a better job of reproducing the surface energy balance budget compared with the CLM5-U3. From Figure 2, we could found that the simulated amplitude and phase of the net radiation (Rn), the sensible heat flux (H), the latent heat flux (LE) and storage heat flux (Q_s) appears to be reasonable, which is closer to observations for CLM5-LCZs than CLM5-U3.

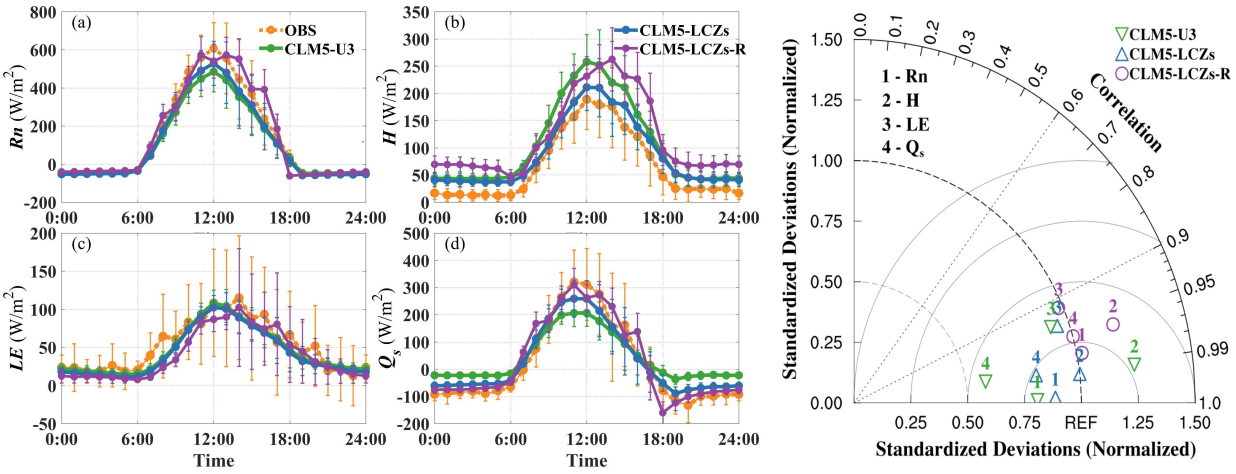

Figure 2. The averaged diurnal cycles of **(a)** net all-wave radiation (*Rn*), **(b)** sensible heat flux (*H*), **(c)** latent heat flux (*LE*), and **(d)** storage heat flux (Q_s) for site observation (orange lines) and two single-point simulations within CLM5 (CLM5-U3, green lines; CLM5-LCZs, blue lines) as well as a regional simulation within CLM5-LCZs (CLM5-LCZs-R) in Nanjing. The Taylor diagram **(e)** exhibits the credibility of the simulations by comparing with site observation.

Compared with observed H, in the CLM5-LCZs case, the daytime peak of H is overestimated by 22.2W m^{-2}, some of which likely results from the deep and narrow street canyons on account of large fractions of LCZ2. The nighttime minimum of H is also overestimated by 26.5W m^{-2} that may be induced by building morphology and materials making more daytime storage heat releases at nighttime (Oleson, Bonan, Feddema, Vertenstein, et al., 2008; W. Zhao et al., 2014). LCZ2 is a dense mix of midrise buildings (3–9 stories) with stone, brick, tile, and concrete construction materials. In tower observations, daytime surface energy balance is dominated by Q_s, which is generally captured by CLM5-LCZs, yet CLM5-U3 can't reappear it. Nevertheless, the deviation between modeled and observed Q_s is relatively larger than other fluxes (Figure 2-e). Observed Q_s is a residual error between Rn and the sum of H and LE, in which some of the anthropogenic heat flux (Q_{ah}) is contained, that partially accounts for the underestimation of Q_s in CLM5-LCZs. Additionally, simulated Q_{ah} (40-55W m^{-2}) in CLM5-LCZs was calculated as heating and air conditioning fluxes by a building energy submodel.

In addition, when the CLM5-LCZs was forced by the China Meteorological Forcing Dataset, surface energy balances derived from a regional simulation were further utilized to evaluate the credibility of it. Figure 2 shows the comparison of simulated fluxes around the tower station (32.03°N, 118.79°E) within this regional simulation and the single-point simulation forced by meteorological observations. It demonstrates that the regional case conducted by CLM5-LCZs with the China Meteorological Forcing Dataset could capture the diurnal fea-

tures of surface energy balance.

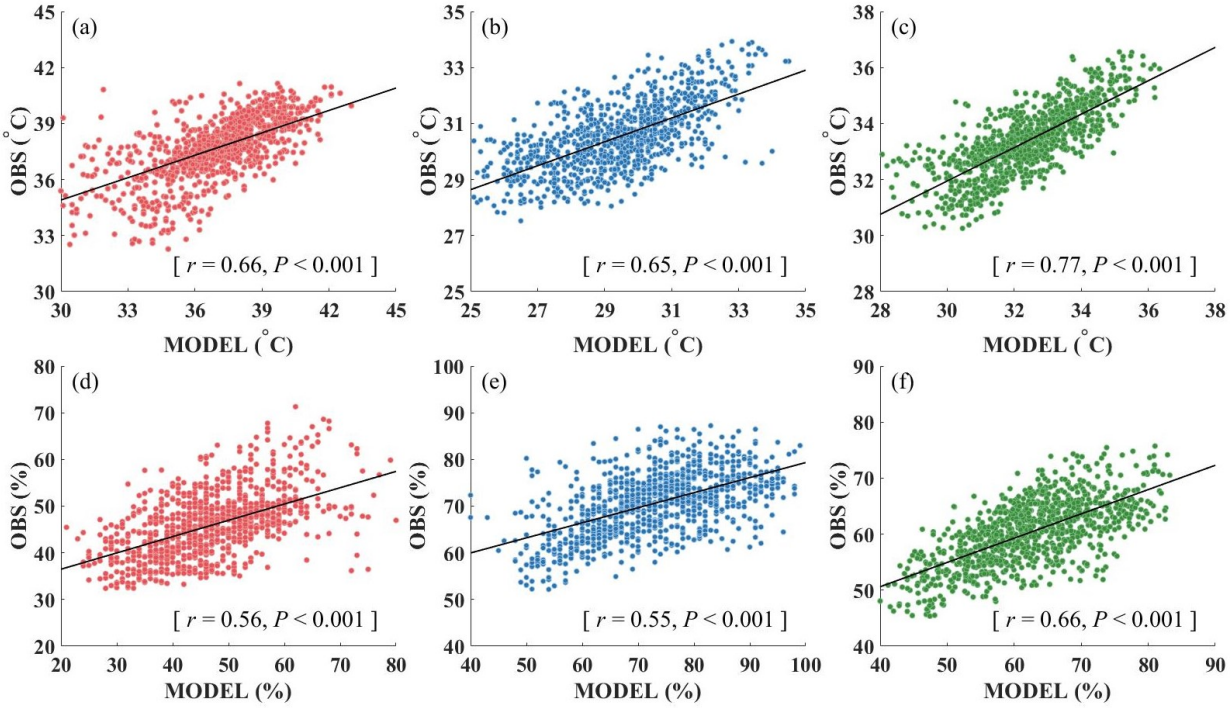

Figure 3. The validation of modeled surface air temperature **(a, b, c)** and relative humidity **(d, e, f)** in selected sites with observational data. **(a), (b)** and **(c)** denote the correlation between modeled and observed daytime, nighttime and daily mean surface air temperature. **(d), (e)** and **(f)** denote the correlation between modeled and observed daytime, nighttime and daily mean relative humidity. The observational data were obtained from 36 automatic weather stations in Nanjing.

Apart from utilizing a tower measurement for the model validation within a single-point case, we also conducted a regional case with a spatial resolution of 1km in Nanjing so as to be compared with observed air temperature and humidity obtained from a measurement network of automatic weather stations. There are several reasons that may account for this model validation using station measurements in Nanjing. First, observations obtained from automatic weather stations in Nanjing have a continuous hourly series including air temperature and relative humidity. Second, these observational data have been cross-checked to correspond to different urban LCZs or rural vegetations through satellite images and field works, which could be utilized not only for the inter-LCZs contrast of temperature or humidity regimes but also for the evaluation of CLM5-LCZs. It is clear that there are acceptable agreements between modeled and observed air temperature (daytime: correlation coefficient, r=0.66, confidence

level, P<0.001; nighttime: r=0.65, P<0.001; daily-mean: r=0.77, P<0.001) and humidity (daytime: r=0.56, P<0.001; nighttime: r=0.55, P<0.001; daily-mean: r=0.66, P<0.001) (Figure 3). These results once again highlight the credibility of the modified model.

3.2 Sensitivity to Urban Heterogeneity

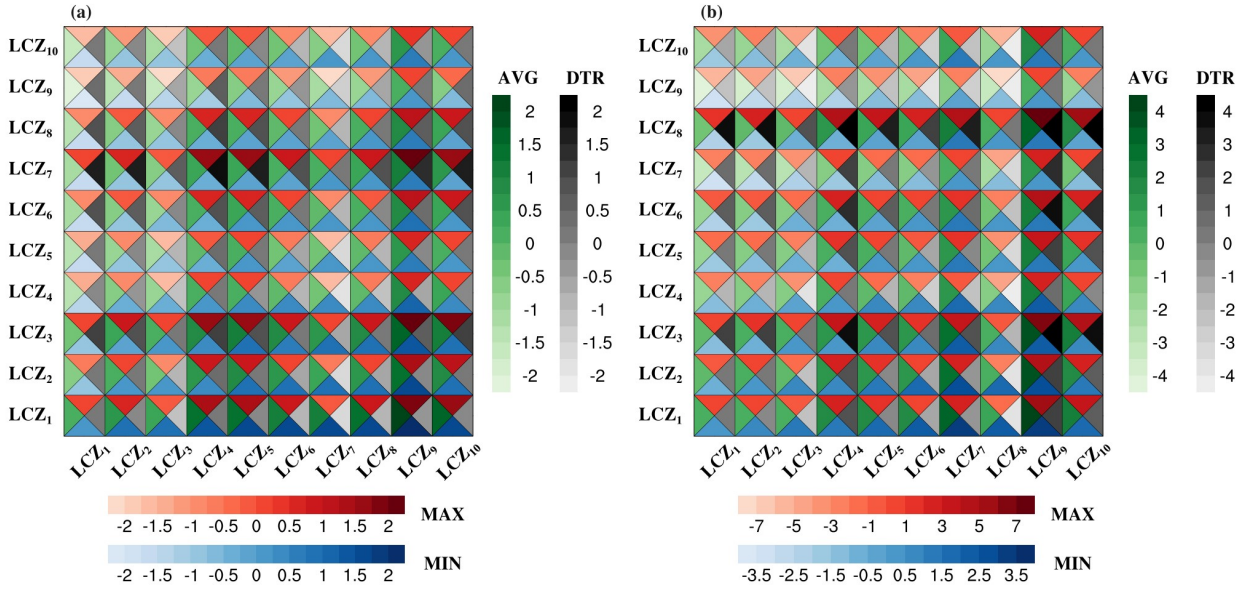

Figure 4. The differential chart of **(a)** surface air temperature (T_a) and **(b)** surface temperature (T_s) for each urban LCZ during a heat wave period in the summer of 2013 in Nanjing. The red (MAX), blue (MIN), green (AVG) and grey (DTR) color table exhibit daytime, nighttime, daily-mean temperature and diurnal temperature range.

With the LCZs scheme, CUHII and SUHII could be calculated in a physically based manner by a temperature difference between urban LCZs and rural lands (i.e., UHII=$T_{LCZ\ x}$-T_r). In this study, rural lands used to match different urban LCZs were consistent over the same grid cells, which are composed of natural land covers (i.e., vegetation, lake and glacier). To examine intra-LCZs variability of UHII, we implemented a single-point case assuming urban lands comprise all urban LCZs. The contrasts of CUHII and SUHII at daytime, nighttime, as well as daily-mean and diurnal temperature ranges among different urban LCZs were exhibited as Figure 4.

During daytime, CUHII is highest in LCZ3, and its differences in LCZ3, LCZ7 and LCZ1 exceed 2 °C each comparing to LCZ9. In terms of urban geometrical morphology alone, the cities with dense and compact buildings (LCZ1~3, the sum of urban building and road fraction exceeds 85%) as well as dense low-rise buildings or roads (LCZ7~8) have a larger CUHII. It indicates urban surface

cover (building and road fraction) plays an important role in daytime CUHII. Nighttime CUHII peaks in LCZ1, and it is also largely explained by the compactness of built-up. Both LCZ1 and LCZ3 have a larger value of daily-mean CUHII (>1.6°C), however, the diurnal range (the difference between maximum and minimum) of CUHII is larger in cities with low-rise buildings (LCZ3, LCZ6, LCZ7 and LCZ8), and its difference between LCZ7 and LCZ10 could reach 1.7 °C that may be induced by the lightweight construction materials of LCZ7 with a high surface albedo and a low thermal conductivity.

Similarly, daytime SUHII is more significant in cities with dense and compact buildings, and the differences exceed 5°C in comparison to sparsely built (LCZ9), and dense buildings imply a larger nighttime SUHII and daily-mean SUHII. A larger diurnal range of SUHII generally coincides with dense low-rise buildings (LCZ3, LCZ6 and LCZ8).

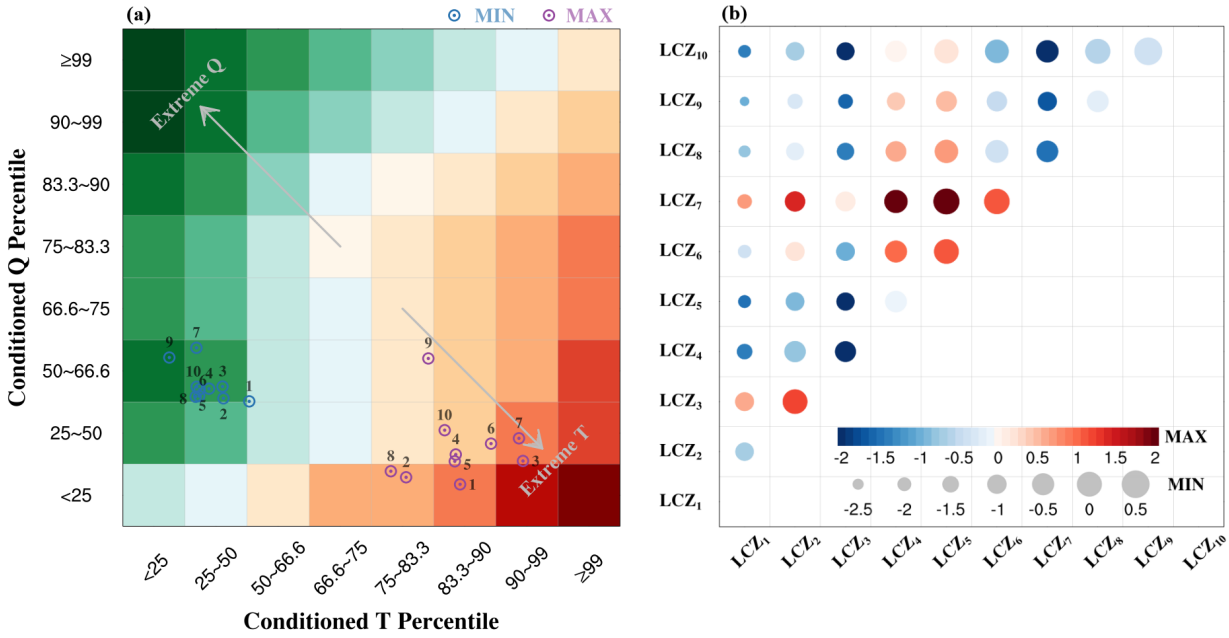

Figure 5. The moist heat stress for each urban LCZ during a heat wave period in Nanjing. **(a)** The surface air temperature (T) – specific humidity (Q) regime plots. The conditional distributions of T and Q were used to represent the exceedance percentile of the heat stress metric comprising both heat and moisture conditions. The purple and blue dots denote daytime (MAX) and nighttime (MIN) T-Q regimes, Extreme T and extreme Q are deep red and deep green, respectively. **(b)** The differential chart of daytime (MAX, the color of circles) and nighttime (MIN, the size of circles) Heat Index (HI) for each urban LCZ.

In order to assess intra-urban heterogeneity of thermal comfort, as mentioned

above, four heat stress metrics with a combination of heat and moist conditions were used for capturing the nonlinearity of the covariation of temperature and moisture conditions (Buzan et al., 2015). Figure 5-a shows the surface air temperature (T) – specific humidity (Q) regime that was calculated by the conditional distribution of T and Q percentile during the HW periods in 2013 that represents threshold percentiles of heat stress metrics. From 5-a and b, we could find that urban dwellers are exposed to a more serious heat stress level in LCZ7 and LCZ3 at daytime, and the cities with an open arrangement of higher buildings (LCZ4 and LCZ5) have a lower heat risk condition, of which the heat index (HI) is less than 2.1°C with respect to LCZ7. Nevertheless, at nighttime, compact buildings (e.g., LCZ1) experience a larger thermal discomfort. In general, during the HW periods, LCZ1 and LCZ3 belong to 'extreme heat' conditions due to a higher daytime heat risk and no relief from accumulative heat stress at nighttime. On the contrary, LCZ5 is in a 'relative low heat risk' condition on account of the minor heat stress at both daytime and nighttime.

4 Urban Heat Islands and Thermal Comfort in East China

4.1 Inter-urban and Intra-urban Variability of UHIs

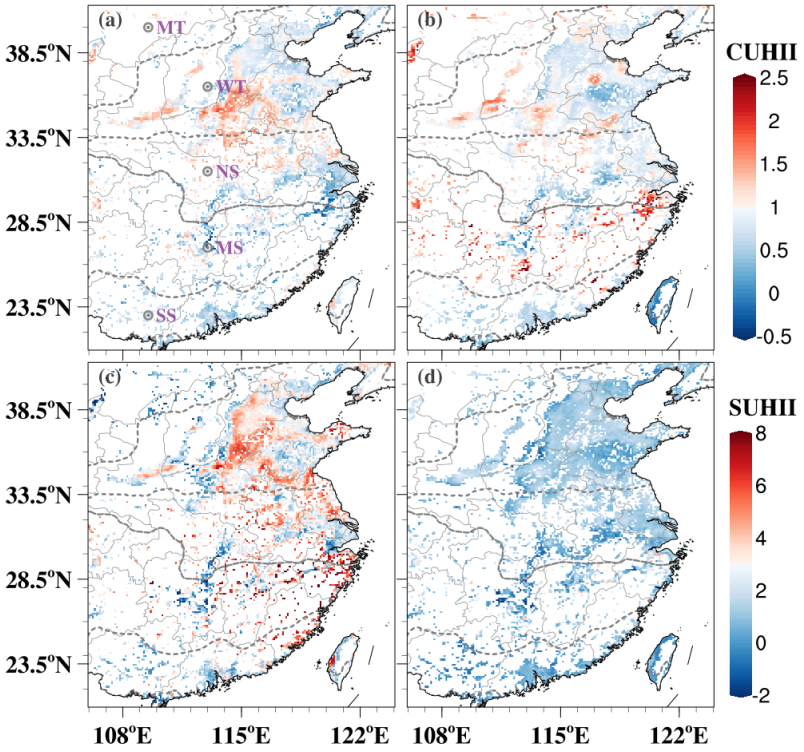

Figure 6. The spatial distribution of averaged canopy urban heat island intensity (CUHII) (**a**, daytime; **b**, nighttime) and surface urban heat island intensity (SUHII) (**c**, daytime; **d**, nighttime) during a heat wave period of 2013 in East

China.

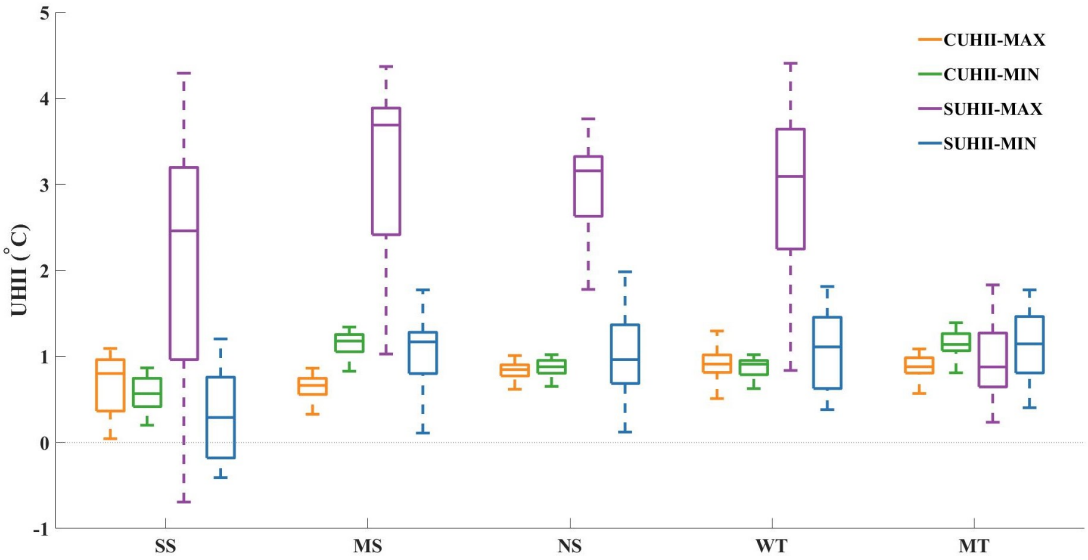

Figure 7. The spatial-mean CUHII and SUHII across SS, MS, NS, WT, and MT climate zones. The orange, green, purple and blue lines denote daytime and nighttime CUHII and SUHII, respectively.

The spatial variations of averaged UHIs across different climate zones during the HW periods are exhibited in Figure 6, in which UHIs are calculated from the LCZs-weighted urban temperatures and the adjacent rural temperatures. It roughly has an increasing trend for daytime CUHII from the southern humid regions to the northern arid regions, and the average over the warm temperate (WT) climate zone reaches up to 0.9°C (Figure 7). Apparently, nighttime CUHII is higher in the mid subtropical (MS) and mid temperate (MT) climate zones (1.1±0.2°C). For daytime SUHII, it peaks in the MS climate zone (3.2±1.0°C), and the north subtropical (NS) and warm temperate (WT) also show a high SUHII (2.9°C). At nighttime, SUHII is obviously lower than daytime SUHII, and it increases along a latitude gradient, reaching the maximum (1.1±0.4°C) in the mid temperate (MT) climate zones.

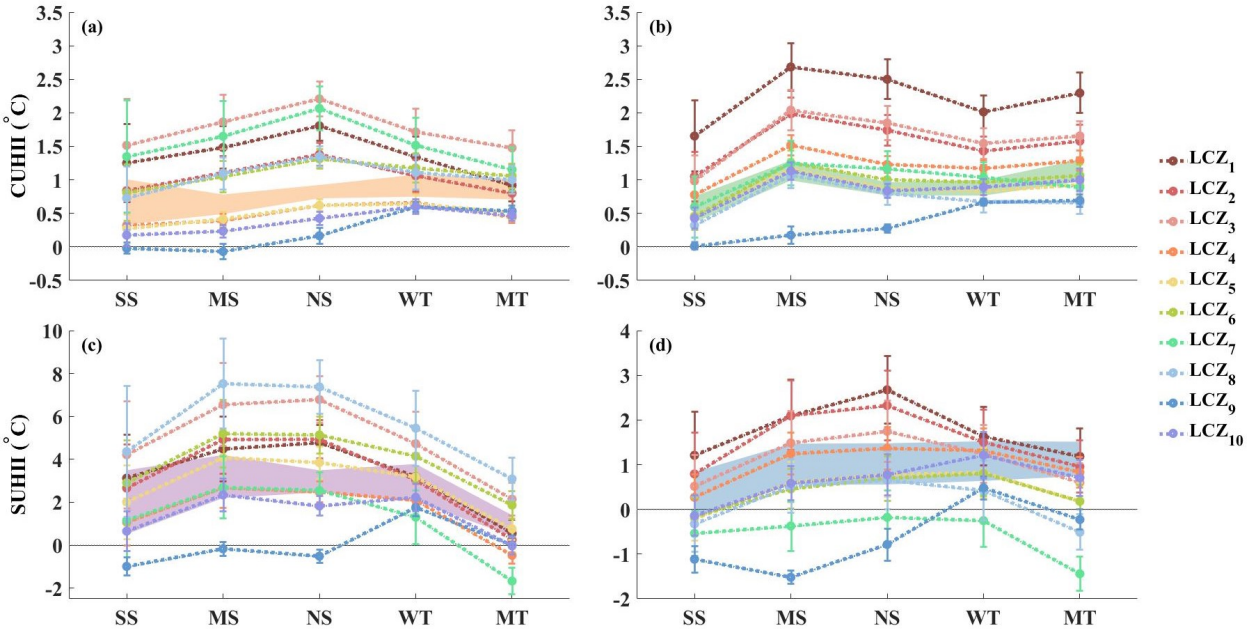

Figure 8. The spatial-mean CUHII (**a**, daytime; **b**, nighttime) and SUHII (**c**, daytime; **d**, nighttime) for each urban LCZ across different climate zones. The orange, green, purple and blue shaded areas denote LCZs-weighted results.

To understand the response of UHIs to the intra-urban inhomogeneity, latitudinal variations of averaged CUHII and SUHII for each urban LCZ, are calculated from the temperature difference between urban LCZs and adjacent rural lands as adopted before (Figure 8). During the daytime, For LCZ1~3 and LCZ6~8, CUHII increases with the latitude first, reaching its maximum in the NS climate zone, and then decreases. However, it shows an increasing trend from south to north for other LCZs. Daytime CUHII is highest in LCZ3 (2.2±0.3°C), LCZ7 and LCZ1 also have a high value. Nighttime CUHII peaks in the MS climate zone for all urban LCZs but LCZ 9. The larger dense and compactness (i.e., LCZ1~3) represent the stronger CUHII at nighttime, especially for LCZ1 (2.7°C in the MS climate zone).

For daytime SUHII, the cities with a large proportion of impervious built-up and low-rise buildings (i.e., LCZ8, LCZ3 and LCZ6) have a stronger UHIs, and daytime SUHII of LCZ8 and LCZ3 are higher in the MS (7.5±2.1°C) and NS (6.8±1.1°C) climate zone among different background climates, respectively. LCZ9 and LCZ10 exhibit a stronger SUHII in the WT climate zone at daytime and nighttime. Nevertheless, the compact building types (i.e., LCZ1~3) have a stronger SUHII at nighttime that is more significant in the NS climate zone, especially for LCZ1 (2.7±0.8°C). Over the MS climate zone, LCZ2 is somewhat higher than LCZ1.

4.2 The response difference of human thermal comfort among urban LCZs

Many heat stress metrics have been developed to estimate thermal comforts, such as the Heat Index (HI) (Rothfusz, 1990), the simplified Wet Bulb Globe Temperature (sWBGT), the Humidex (HUMIDEX), and the Temperature Humidity Index for Physiology (THIP) (Buzan et al., 2015):

$$HI = -8.7847+1.6114T_a-0.012308T_a^2+RH\left(2.3385-0.14612T_a+2.2117\times10^{-3}T_a^2\right)$$

$$+RH^2(-0.016425+7.2546\times10^{-4}T_a-3.582\times10^{-6}T_a^2), \quad (1)$$

$$sWBGT = 0.56T_a + \frac{0.393e_{RH}}{100} + 3.94, \quad (2)$$

$$HUMIDEX = T_a + \frac{5}{9}\left(\frac{e_{RH}}{100}-10\right), \quad (3)$$

$$THIP = 0.63T_w + 1.17T_a + 32, \quad (4)$$

where T_a, RH, e_{RH} and T_w denote air temperature (°C), relative humidity (%), vapor pressure (mb), and Wet bulb temperature (°C), respectively. These metrics are the combination of temperature and humidity that could more realistically assess human-perceived heat stress (Mishra et al., 2020; Zhao et al., 2021). HI is a feels-like moist heat metric based on the comfort algorithms, and 40–51 °C is danger, and 52 °C is extreme danger. sWBGT is used to estimate heat stress in sports medicine based on the empirical algorithms. It is unitless and 32.2 is a dangerous condition. HUMIDEX is unitless that also based on the comfort algorithms, and 46-53 is dangerous, and 54 is imminent heat stroke. THIP is designed for direct physiological responses within humans and animals based on the physiology algorithms, and 79–89 is dangerous, and 90 is very dangerous. In CLM, a module of heat stress indices has been developed to study the interactions between urban effect, climate warming, heat wave and heat stress (Buzan et al., 2015; Oleson et al., 2015). By utilizing this module, intra-LCZ variability of thermal comfort level could be investigated.

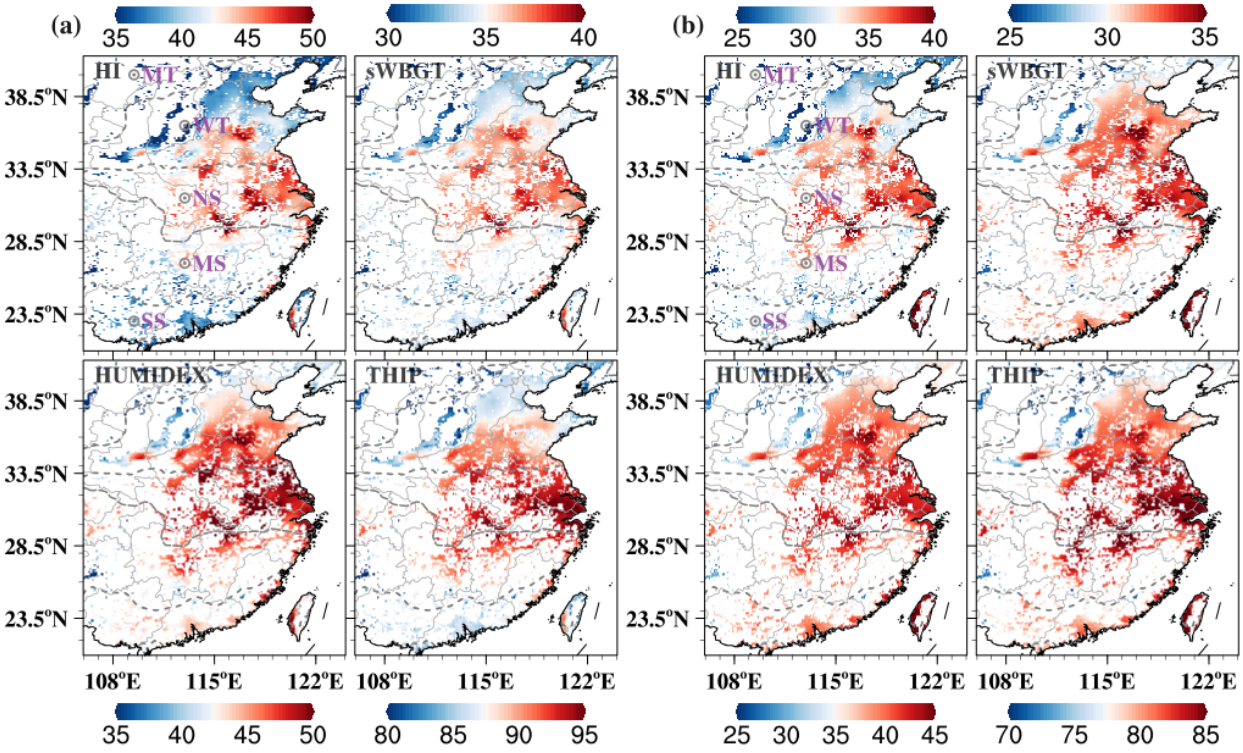

Figure 9. The spatial distribution of averaged heat stress metrics, including HI, sWBGT, HUMIDEX and THIP in cities at daytime **(a)** and nighttime **(b)** during the HW periods.

Considering the different behaviors in thermal comfort within cities, four heat and moist metrics including the Heat Index (HI), the simplified Wet Bulb Globe Temperature (sWBGT), the Humidex (HUMIDEX) and the Temperature Humidity Index for Physiology (THIP), to evaluate heat stress for all urban LCZs. Figure 9 depicts spatial variations of these metrics derived from the weighted average of each LCZ at daytime and nighttime during the HW periods. At first glance, it is in a remarkable heat risk condition over the NS climate zone. The spatial patterns of these metrics are roughly consistent, yet the high-value area of heat stress is more located in the Yangtze River Delta agglomeration for THIP and other metrics are not.

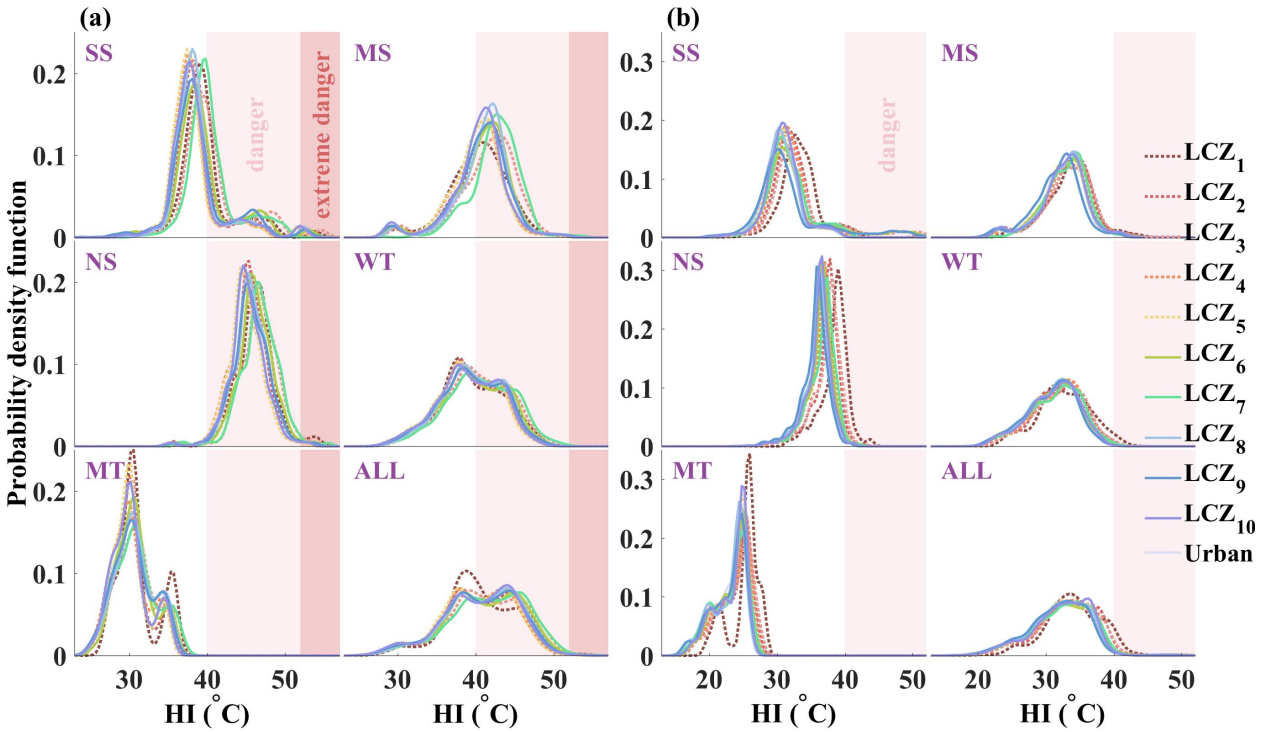

Figure 10. The probability distribution functions of **HI** for each urban LCZ and LCZs-weighted (Urban) in SS, MS, NS, WT, MT climate zones and the whole domain (ALL) at daytime **(a)** and nighttime **(b)** during the HW periods. The light pink and red areas denote urban heat stress levels are danger (40~51 ℃) and extreme danger (52 ℃), respectively.

Specifically, we utilized the probability density functions (PDF) of HI to examine the relationship between urban features and heat stress across different climate zones (Figure 10). Given the levels of discomfort based on a scale for determining heat stress: 40–51 °C is danger, and 52 °C is extreme danger. Urban dwellers are easily exposed to a serious heat stress in the NS climate zone because almost all cities (~98%) are with a danger heat level at daytime, of which 1% are in extreme danger. Meanwhile, people could not get a relief from heat on account of a high HI at nighttime. By contrast, in the SS climate zone, there are a few cities situated in an extreme danger conditions even at nighttime. The phase and amplitude of PDF for each urban LCZs are roughly similar. LCZ3, LCZ7 and LCZ1 experience a more significant heat discomfort at daytime. Additionally, at nighttime, the compact building types (i.e., LCZ1~3) correspond to a higher heat stress, and 23% of LCZ1 are within a danger heat risk.

4.3 The Impacts of HW on UHIs and Urban Heat Stress

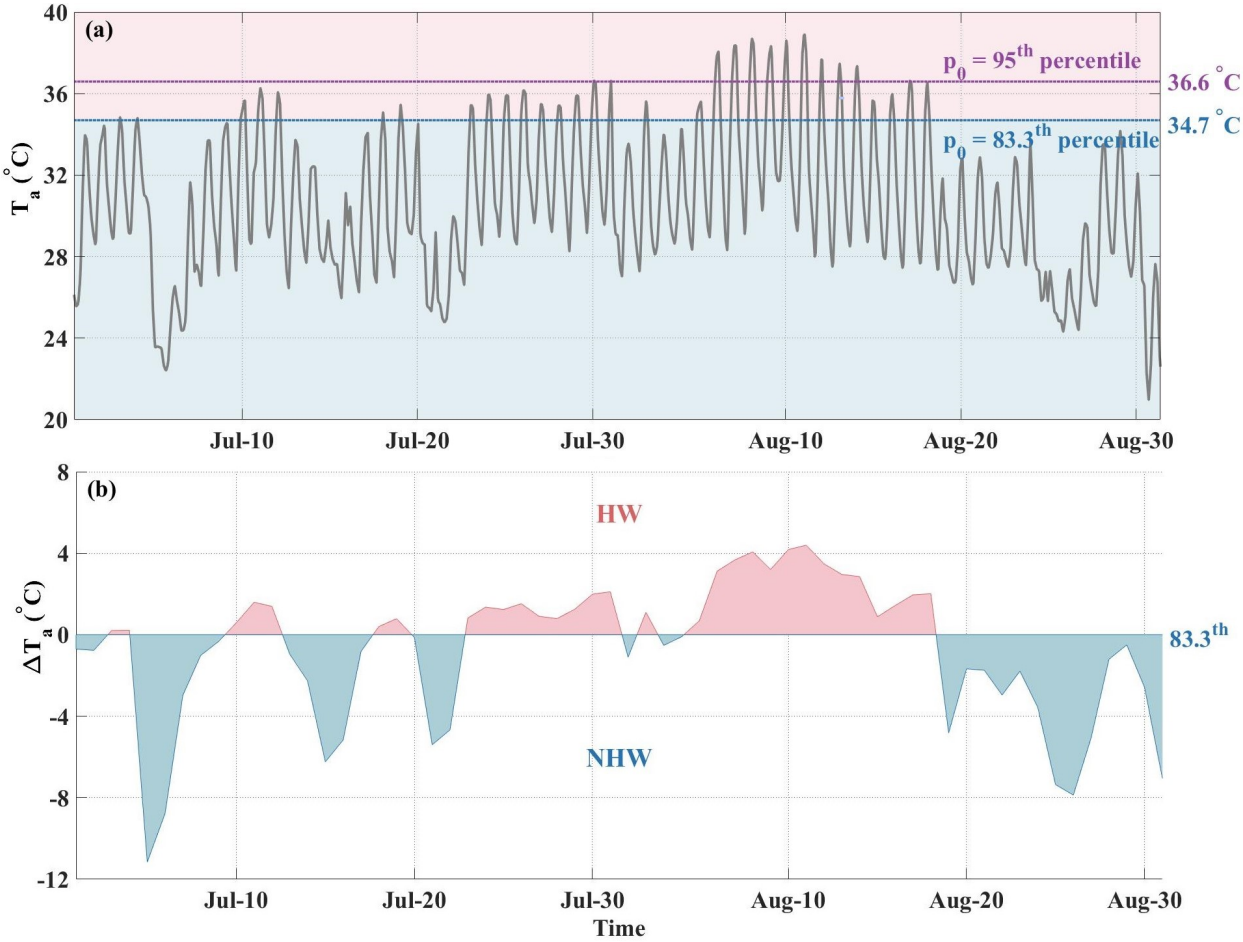

Figure 11. The definition of heat wave (HW) and non-heat wave (NHW) periods. **(a)** The time series of daily T_a from 1 July to 31 August in 2013. p_0 is the percentiles of a total of 828 summer days during 2010-2018 that represent the threshold to identify HW and NHW days. **(b)** The T_a departure based on a temperature threshold of 83.3th percentile (34.7 ℃), HW and NHW days are represented with red and blue areas, respectively.

A percentile threshold method was implemented to define the occurrence of the HW based on a certain percentile of temperature observations (Luo & Lau, 2017; Miao et al., 2022). It is suitable to investigate the synergistic interactions between UHIs and HW at a large scale with different background climates. We utilized the 2-m daily maximum T_a in a total of 828 summer days during 2010-2018 to determine the threshold percentile (i.e., p_0). A HW day was identified if maximum T_a reaches the predetermined p_0. For instance, if p_0 was the 83.3th percentile and 95th percentile that corresponds to the temperature threshold of 34.7 ℃ and 36.6 ℃, a total of 31 HW days and 13 HW days were identified during

the summer (July-August, a total of 62 summer days) in 2013, respectively (Figure 11). The variations of p_0 represent different HW intensities. Meanwhile, the NHW days were identified with a fixed percentile threshold (i.e., the 83.3^{th} percentile) under various HW intensities. There are a total of 31 NHW days ($p_0 < 83.3^{th}$, the blue area in Figure 11) during the summer (July-August) in 2013.

Given the compound heat extremes caused by UHIs and HW (Shi et al., 2021; Wu et al., 2021), we analyzed the impact of HW on CUHII and SUHII as well as the controlling factors of SUHII using the difference between HW and NHW periods. It could be described as follows:

$$I_C = \frac{1}{n_1}\sum_1^{n_1} CUHII_{HW} - \frac{1}{n_2}\sum_1^{n_2} CUHII_{NHW} = \frac{1}{n_1}\sum_1^{n_1}(T_{a,u,HW} - T_{a,r,HW}) - \frac{1}{n_2}\sum_1^{n_2}(T_{a,u,NHW} - T_{a,r,NHW}) \quad (5)$$

$$I_S = \frac{1}{n_1}\sum_1^{n_1} SUHII_{HW} - \frac{1}{n_2}\sum_1^{n_2} SUHII_{NHW} = \frac{1}{n_1}\sum_1^{n_1}(T_{s,u,HW} - T_{s,r,HW}) - \frac{1}{n_2}\sum_1^{n_2}(T_{s,u,NHW} - T_{s,r,NHW}) \quad (6)$$

where I_C and I_S separately denote the changes in CUHII and SUHII between HW and NHW periods. n_1 and n_2 are the numbers of HW and NHW days defined by the temperature threshold method during the summer in 2013, respectively. $T_{a,u,HW}$, $T_{a,r,HW}$, $T_{a,u,NHW}$ and $T_{a,r,NHW}$ represent urban and rural air temperatures in HW and NHW days, and $T_{s,u,HW}$, $T_{s,r,HW}$, $T_{s,u,NHW}$ and $T_{s,r,NHW}$ are for surface temperatures.

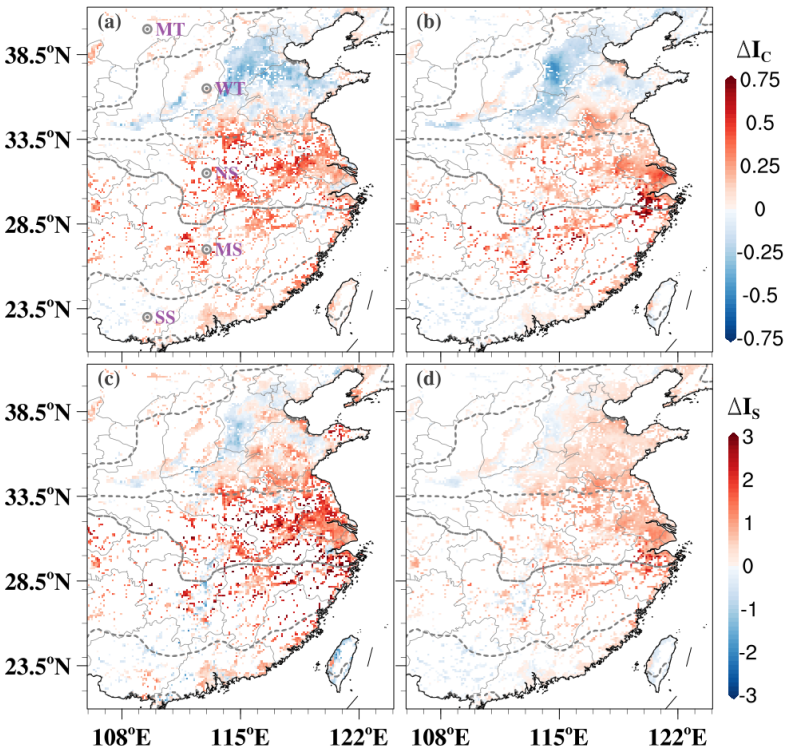

Figure 12. The spatial distribution of averaged changes in CUHII (I_C) and SUHII (I_S) between HW and NHW periods in East China. (**a**), (**b**) daytime and nighttime I_C, (**c**), (**d**) daytime and nighttime I_S.

To investigate the role of the occurrence of HW in UHIs, we utilized the changes in CUHII (I_C) and SUHII (I_S) between HW and NHW periods. Here HW and NHW periods were identified by the temperature threshold of 34.7°C (i.e., the 83.3th percentile). As Figure 12 shows, the intensification of HW on CUHII and SUHII generally exhibits a decreasing trend from the humid to arid regions at both daytime and nighttime. More specifically, the I_C is mostly a negative value in the WT climate zone and a small negative value in the west of SS climate zone, while it is greater than 0 in other climate zones. The I_S nearly represent a positive value apart from some areas in the WT climate zone (Miao et al., 2022). These results demonstrate CUHII and SUHII are mostly magnified by HW in the humid regions, however, HW weakens daytime and nighttime CUHII as well as daytime SUHII in the arid

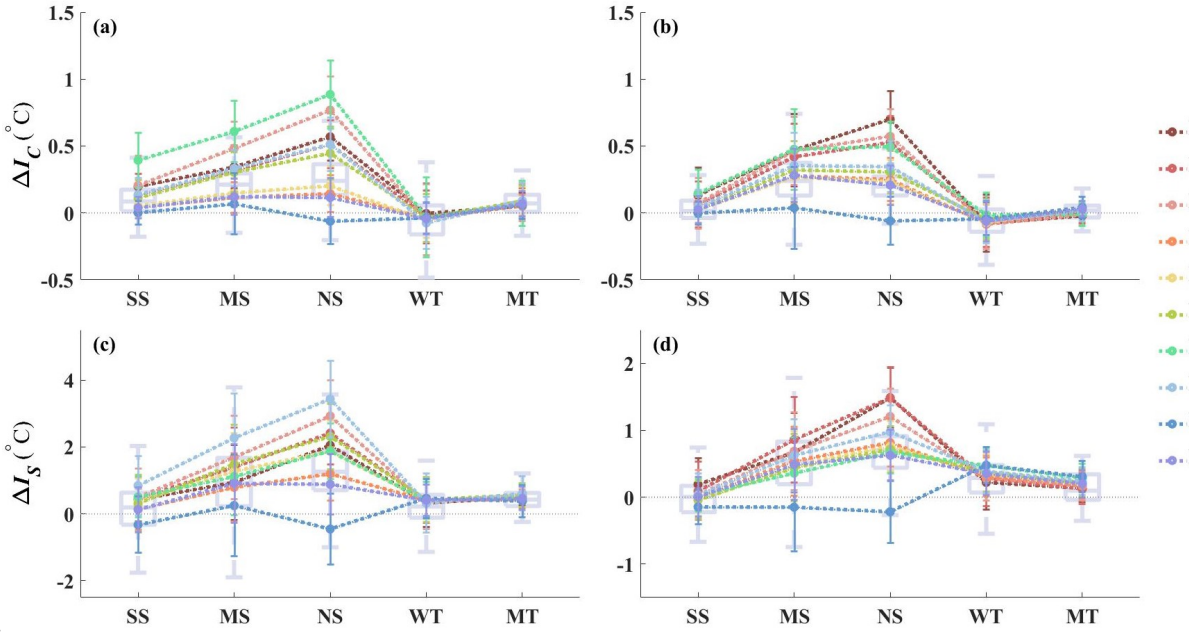

regions.

Figure 13. The spatial-mean I_C (**a**, daytime; **b**, nighttime) and I_S (**c**, daytime; **d**, nighttime) for each urban LCZ across different climate zones. The grey boxes denote LCZs-weighted results.

With respect to each urban LCZ, both I_C and I_S generally increase with the latitude first, peaking in the NS climate zone, and then reaching the minimum in the WT climate zone (Figure 13). At daytime, the impacts of HW on LCZ7 and LCZ3 are more significant, and it reaches 0.9 and 0.8 °C in the NS climate zone, respectively. Nighttime I_C is larger for the cities with compact buildings (i.e., LCZ1~3) and LCZ7, and LCZ1 is easier affected by HW (0.7±0.2°C). In the WT climate zone with a relatively arid condition, CUHII of all urban LCZs are weakened by HW at daytime and nighttime. Both I_C and I_S are negative for LCZ9 in the NS climate zone. For daytime SUHII, the cities with a high proportion of impervious surface and low-rise buildings are significantly magnified by HW (2.9°C for LCZ8, in the NS climate zone). Nighttime I_S is more likely to be strengthened for the compact building types (1.5°C for LCZ1 and LCZ2, in the NS climate zone).

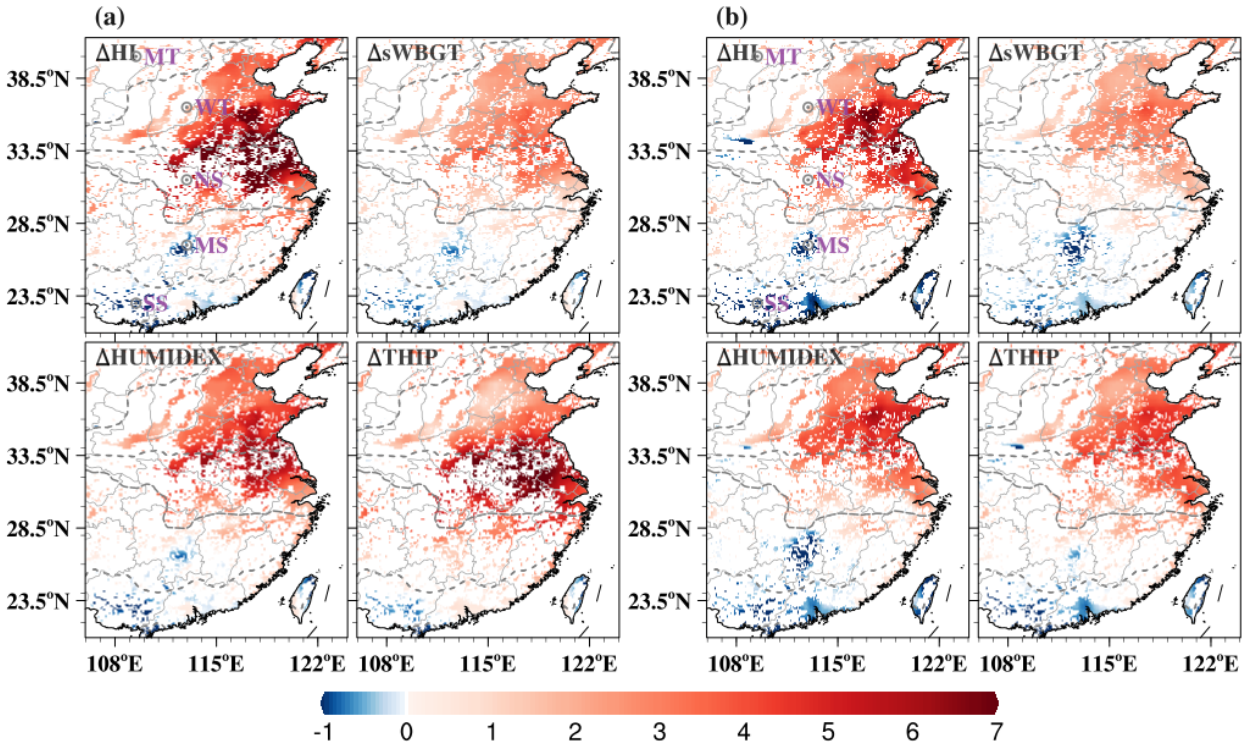

Figure 14. The spatial distribution of averaged changes in four heat stress metrics (HI, sWBGT, HUMIDEX and THIP) between HW and NHW periods at daytime (**a**) and nighttime (**b**) in East China.

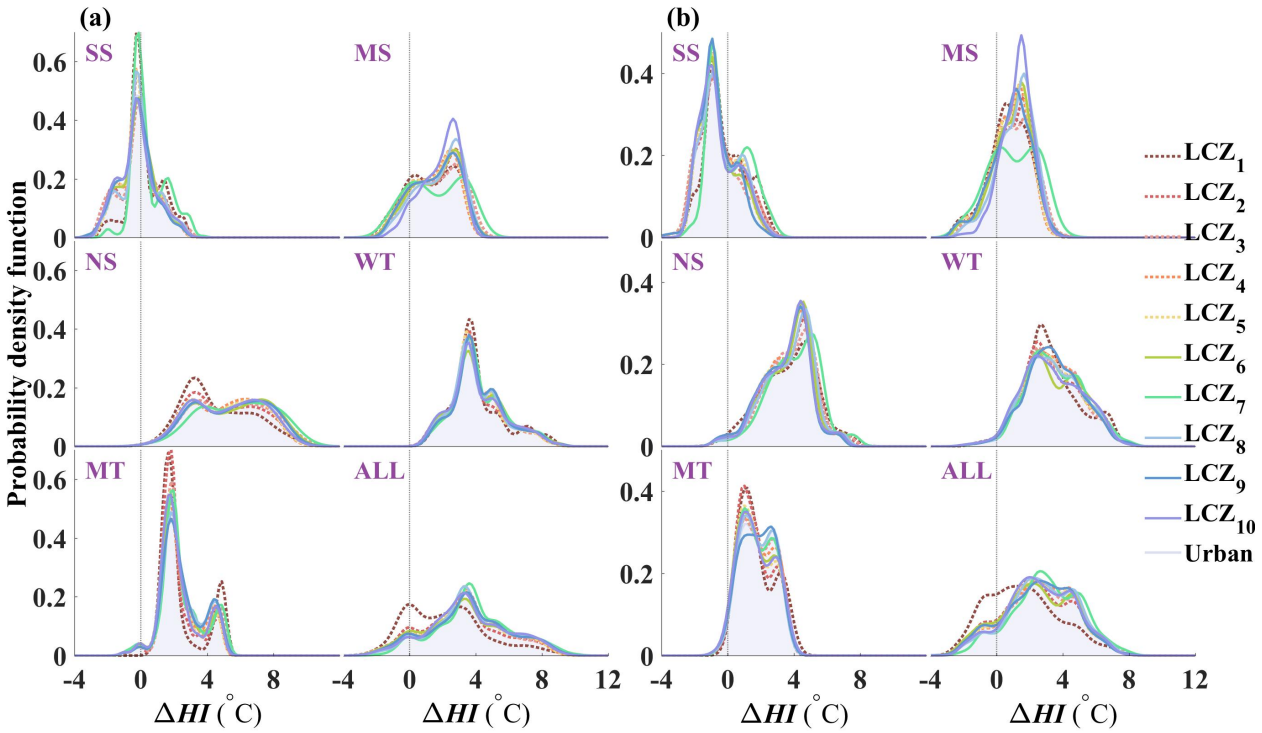

Figure 15. The probability density functions of HI for each urban LCZ and LCZs-weighted (Urban) in SS, MS, NS, WT, MT climate zones and the whole domain (ALL) at daytime **(a)** and nighttime **(b)**.

Figure 14 exhibits the spatial distributions of the changes in heat stress metrics including HI, sWBGT, HUMIDEX and THIP between HW and NHW periods for LCZs-weighted results. we find that the occurrence of HW deteriorates the thermal comfort in relatively arid regions (i.e., in the NS, WT and MT climate zones), which is more notable for the HI metric in the NS climate zone (58% of cities have a HI more than 5 °C, see Figure 15). However, urban heat risks are alleviated by the HW in most parts of SS climate zone and south-central of MS climate zone. In particular, at nighttime, the peak value of the probability density function of HI is approximately -0.9°C, and the thermal environments for about 50% of cities are improved by more than 0.9°C.

Specially, at daytime, the occurrence of HW reduces the heat risk more easily in cities with open build types (LCZ4~6) or a high proportion of pervious roads (LCZ9~10, about half of which are covered by vegetation and unsurfaced road) in the SS climate zone. This effect for LCZ7 and LCZ1 is relatively weaker. On the contrary, for a small part of regions in the MS climate zone, LCZ 1 and LCZ7 get more benefits from HW. At nighttime, the cities composed of low-rise buildings (LCZ3, LCZ6 and LCZ9) get more relief from heat stress in the SS climate zone when the HW occurs. In northern climate zones with

a relatively arid condition, the HW worsens the heat environment, especially for the building types with low-rise buildings and high fractions of impervious surfaces (i.e., LCZ3, LCZ6, LCZ7 and LCZ8).

4.4 The Attribution of SUHII

Recent works devoted to identifying the causes of surface UHIs were conducted by the attribution method including the intrinsic biophysical mechanism (IBM) method (L. Zhao et al., 2014) and the two-resistance mechanism (TRM) method (D. Li et al., 2019). These methods are based on the first-order Taylor series expansion of a linearized surface energy balance equation ($Rn+Q_{ah}=H+LE+Q_s$), where $Rn=S_{\downarrow}+L_{\downarrow}-S_{\uparrow}-L_{\uparrow}$ is the net all-wave radiation, $S_{\downarrow}$ and $S_{\uparrow}$ denote the downward and upward shortwave radiation, respectively, $L_{\downarrow}$ and $L_{\uparrow}$ represent downward and upward longwave radiation, respectively, and Q_{ah}, H, LE, and Q_s denote anthropogenic heat flux, sensible heat flux, latent heat flux and heat storage, respectively. As demonstrated in C. Li and Zhang (2021), both two methods indicate the dominant factor of spatial variations of UHI intensity is the urban-rural contrast of evaporation efficiency, which is modulated by a rural landscape. Therefore, in this study, the IBM method was utilized to estimate intra-urban variability of attributing factors of SUHII and the impacts of HW intensity and local climate on dominant factors.

The IBM method could be described as (the model details see C. Li and Zhang (2021)):

$$T_s = \left(\frac{T_s}{R_n^*}\right) R_n^* + \left(\frac{T_s}{r_a}\right) r_a + \left(\frac{T_s}{\quad}\right) \quad + \left(\frac{T_s}{Q_s}\right) Q_s + \left(\frac{T_s}{Q_{ah}}\right) Q_{ah} \quad (7)$$

where T_s is the change in surface temperature induced by land-use perturbation. Considering the effect of urbanization, $T_s=T_{s,u}-T_{s,r}$ represents SUHII ($T_{s,u}$ and $T_{s,r}$ denote urban and rural surface temperatures, respectively). R_n^*, r_a, , Q_s and Q_{ah} represent the apparent net radiation, the aerodynamic resistance, the Bowen ratio, the heat storage and anthropogenic heat flux, respectively. In equation (7), five terms successively indicate contributions to SUHII from the urban-rural contrast of net radiation, the efficiency of convecting heat from the surface to the lower atmosphere, evapotranspiration, heat storage and anthropogenic heat.

Here, a weighted approach was applied to calculate the partial derivatives (e.g., $\left(\frac{T_s}{R_n^*}\right)$) in the equation (7) based on urban and rural variables. That could be described as follows:

$$D = \frac{D_r + mD_u}{1+m} \quad (8)$$

Where D denotes the final partial derivatives within the attribution, D_u and D_r denote the partial derivatives calculated separately using rural or urban variables, respectively. m is weight coefficient, which was optimized by minimizing the root-mean-square-error between modeled and attributed SUHII. Given the attribution of SUHII in East China, the optimal value for m is 4.2 and 1.9 at

daytime and nighttime, respectively (Figure 16).

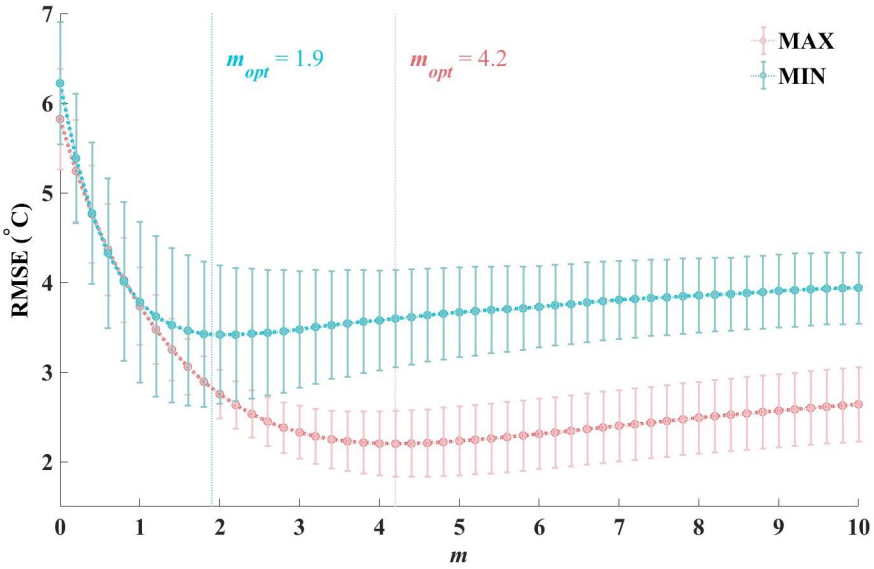

Figure 16. The optimization of $\boldsymbol{m}$ to calculate the derivative terms in the IBM attribution methods during the daytime (MAX, light blue line) and nighttime (MIN, light red line) by minimizing the RMSE between modeled and attributed SUHI intensity. m_{opt} is the optimal value for $\boldsymbol{m}$.

As mentioned above, the IBM method was used to isolate the causes of SUHII, and then to explore the impacts of intra-urban heterogeneity on SUHII and its controlling factors. These factors contain the changes in net radiation (Rn), the efficiency convecting heat from the surface to the lower atmosphere (r_a), the evaporative cooling rate ( ), heat storage (Q_s) and anthropogenic heat (Q_{ah}) between each urban LCZ and adjacent rural areas. Furthermore, to investigate the effect of HW intensity on SUHII and its controlling factors (i.e., I_{Rn}, I_{r_a}, I , I_{Q_s} and $I_{Q_{ah}}$), HW days in different temperature levels (i.e., the temperature percentile, p_0) were utilized to compare with NHW days that defined by a fixed p_0 (the 83.3th percentile, corresponding to 34.7 ℃).

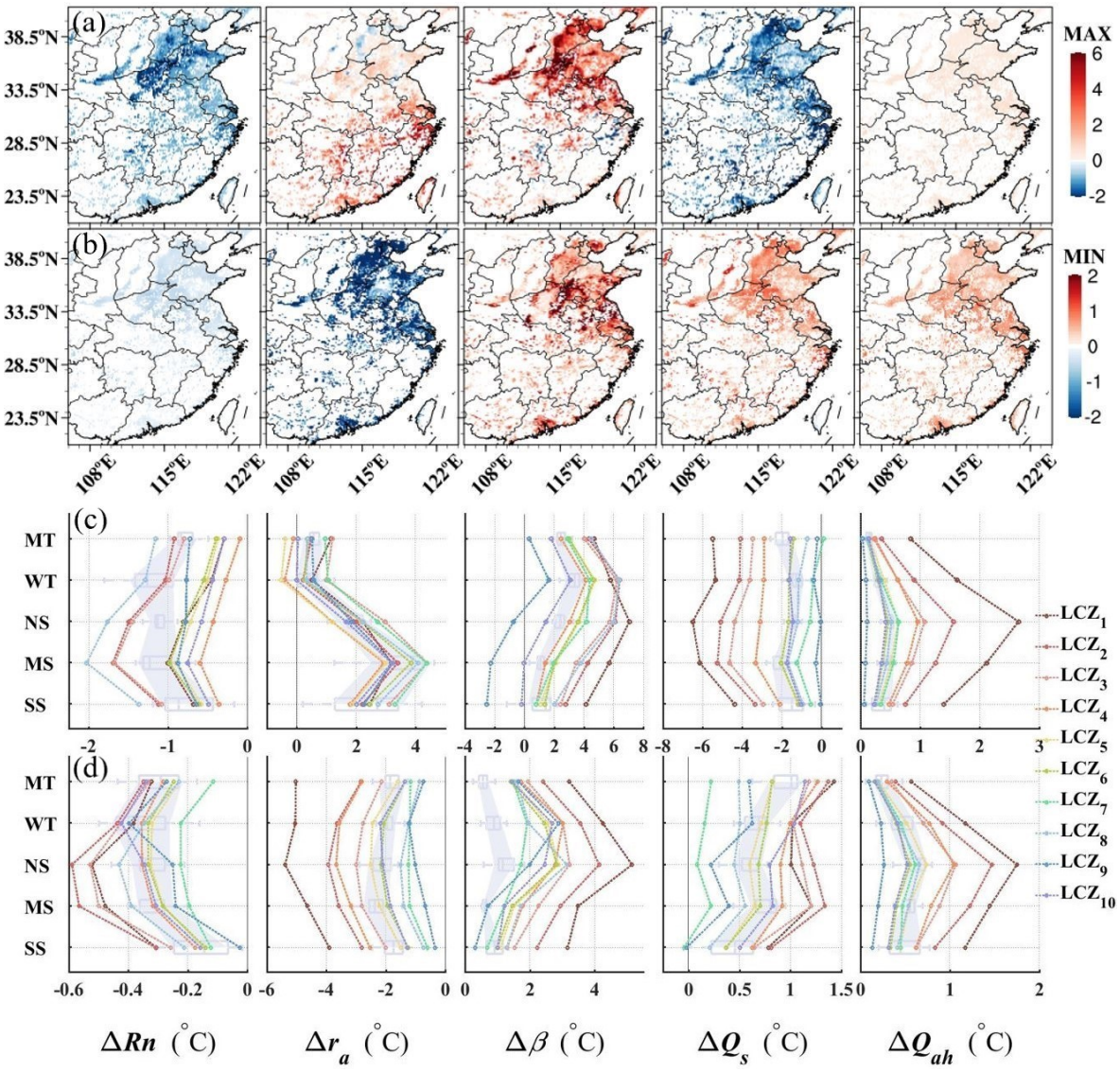

Figure 17. The quantitative attribution of the various contributions to SUHII from controlling factors obtained by the intrinsic biophysical mechanism (IBM) method. The spatial distribution of various contributions to SUHII at daytime **(a)** and nighttime **(b)** during the HW periods in East China. The latitudinal variations in various contributions to SUHII for each urban LCZ and LCZs-weighted (grey areas) at daytime **(c)** and nighttime **(d)**. The latitudes increase gradually in SS, MS, NS, WT, and MT climate zones. Rn, r_a, , Q_s and Q_{ah} represent contributions from the urban-rural contrast of net radiation, aerodynamic resistance, Bowen ratio, heat storage and anthropogenic heat.

At daytime, the spatial variations of SUHII are dominated by in the arid northern region (e.g., 3.4℃ in the WT climate zone) and r_a in the humid southern region (e.g., 3.5℃ in the MS climate zone) during a heat wave period (Figure 17). Q_s and Rn weakens SUHII, and this effect is -2.1℃ for Q_s in the MS climate zone and -1.2℃ for Rn in the WT climate zone. Q_{ah} somewhat strengthens SUHII by 0.5℃ in the NS climate zone. However, at nighttime, r_a significantly restrains SUHII (~-2℃), while SUHII is largely strengthened by in the SS, NS, WT climate zone (~1℃), and largely strengthened by Q_s in the MS and MT climate zone.

Given the intra-variability of controlling factors, the latitudinal variations almost exhibit as a consistent trend for all urban LCZs. At daytime, the contribution of r_a show a decreasing trend from humid to arid regions, yet increases. Notably, the impact of urban features on r_a contribution (~2℃) is obviously less than the role of background climates (~4℃), whereas other factors are more easily affected by intra-urban heterogeneity and local climates play a regulating role. The city with an open arrangement of relatively high buildings (LCZ4~5) signifies that it could convect surface heat to the atmosphere more efficiently, thus reducing SUHII. The city with low-rise buildings and a large fraction of impervious surfaces (LCZ 3, LCZ7) has a larger r_a contribution. For contribution, it is larger in compact types (LCZ1~3) and LCZ8 due to lacking in pervious roads used to evaporate water, while LCZ9 shows a negative contribution in humid regions. In addition, the roles of Q_s and Q_{ah} are also notable in compact types. At nighttime, Q_s contribution roughly increases with latitude, yet other terms reach their maximum in the NS climate zone. The height of buildings (e.g., LCZ1, LCZ2, LCZ4) plays a remarkable role in the inhibiting effect of r_a on SUHII, whereas for other factors, the dense and compactness of buildings (i.e., LCZ1~3) are of great importance.

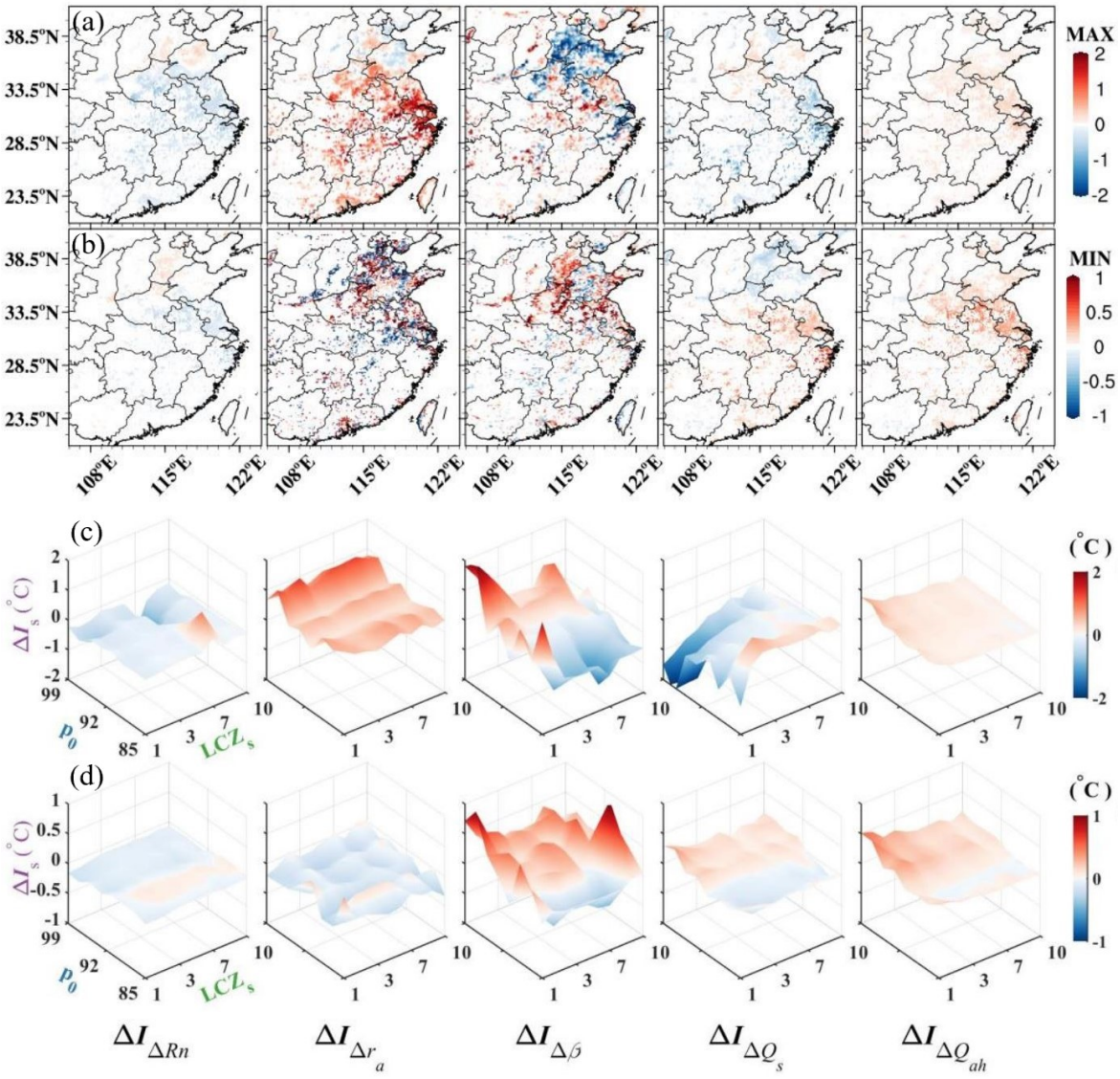

Figure 18. The impact of HW intensity on various contributions to SUHII from five controlling factors (I_{Rn}, $I_{\mathrm{r_a}}$, I , $I_{\mathrm{Q_s}}$ and $I_{\mathrm{Q_{ah}}}$). $\mathrm{p_0}$ is the threshold percentiles to identify HW and NHW days. The spatial distribution of I_{Rn}, $I_{\mathrm{r_a}}$, I , $I_{\mathrm{Q_s}}$ and $I_{\mathrm{Q_{ah}}}$ at daytime **(a)** and nighttime **(b)** with a temperature threshold of 83.3$^{\mathrm{th}}$ percentile (34.7 ℃) in East China. The changes in averaged contributions between HW and NHW periods for each urban LCZ vary with $\mathrm{p_0}$ (i.e., HW intensity) at daytime **(c)** and nighttime **(d)**.

Figure 18-a and b depict the spatial distributions of the changes in controlling factors between HW ($\mathrm{p_0}$ 83.3$^{\mathrm{th}}$) and NHW ($\mathrm{p_0}$<83.3$^{\mathrm{th}}$) periods. At daytime,

the effects of HW on r_a and decrease with latitude for most of the climate zones except for the MT climate zone. I_{Rn} and I_{Q_s} show an increasing trend from the humid southern regions to the arid northern regions, and Rn and Q_s are enhanced by the occurrence of HW in the relatively arid regions, especially for WT climate zone. Daytime and nighttime $I_{Q_{ah}}$ reaches its maximum in the NS climate zone. Nighttime I_{Rn} has a similar trend as daytime, whereas the effects of HW on Q_s decrease from the humid to the arid regions that is in contrast to daytime. At nighttime, I_{r_a} peaks in the SS climate zone and reaches its minimum in the MS climate zone, and the minimum of I is also in the MMS climate zone, and its peak is in the NS climate.

To evaluate the response of these controlling factors for different urban LCZs to HW intensity, we utilize the slope of the linear fits (i.e., I_{slope}, the unit is ℃/p_0) for the changes in factors with the HW intensity (i.e., the temperature threshold, p_0). At daytime, the intensifications of r_a, and Q_{ah} to LCZs-weighted SUHII gradually increase with HW intensity, and I_{slope} of them are 0.03℃/p_0, 0.05℃/p_0 and 0.01℃/p_0, while I_{slope} of Rn and Q_s are -0.03℃/p_0, -0.06℃/p_0. At nighttime, the positive contributions of and Q_s increase with HW intensity with a slope of 0.02℃/p_0 (Figure 18-c and d).

For different urban LCZs, daytime I_{slope} of r_a is larger in the arid northern regions, especially for LCZ3, yet it is smaller in the humid southern regions where LCZ5 has a high value and LCZ3 has a low value. The amplitudes among urban LCZs vary from 0.01 ℃/p_0 to 0.06℃/p_0 across several climate zones, that is less than the changes in local climates (0.07℃/p_0). Daytime I_{slope} of also increases with latitude, and the ranges of it on account of urban features (0.15℃/p_0) exceed local climates (0.10℃/p_0). At nighttime, I_{slope} of r_a is positive in the NS climate zone, whereas it is a notably negative value in the MS climate zone. Additionally, the effects of HW intensity on r_a have a similar variation range between urban features and local climates (~0.05℃/p_0). The variations for I_{slope} of induced by intra-urban heterogeneity (0.09℃/p_0) is larger than background climates (0.04℃/p_0), both of which are comparable for I_{slope} of Q_s (~0.02℃/p_0).

4 Conclusions and Discussion

It is crucial to investigate the interactions among climate change, UHIs and extreme heat for addressing urban climate risks at a global scale and to make urban areas globally comparable, whereas it is restricted by the absence of urban representation in global-scale earth system models (Zhao et al., 2021) and lacking in appropriate uniform global-scale data for urban form and cover (Jackson et al., 2010; Qian et al., 2022). The up-to-date CESM is an extensively used and validated global climate model that has a physically based urban land parameterization (CLMU) as parts of land component (CLM5). It only utilizes the TBD, HD and MD urban extent, datasets of which have a notable national difference, and thermal and radiative properties could not be captured. Nevertheless, the LCZs framework could play an important role in the studies of UHIs, urban heat mitigation and planning, as well as standardizing the worldwide exchange

and communication of urban climate. Therefore the LCZs scheme is incorporated into CLMU-CLM5 to further describe the intra-urban heterogeneity. In addition, the corresponding LCZs map and parameters are applied for the simulations. By comparing with observations obtained from a tower measurement and many automatic meteorological stations, it demonstrates that there is a good simulation performance.

The intra-urban variabilities of UHIs and urban thermal comfort are investigated across different climate zones during a HW period that is defined by the temperature threshold in East China. It roughly has an increasing trend for daytime CUHII and nighttime SUHII from the southern humid regions to the northern arid regions. Nighttime CUHII and daytime SUHII is higher in the mid subtropical (MS) climate zone (1.1±0.2°C and 3.2±1.0°C). Daytime CUHII is highest in LCZ3 (2.2±0.3°C). The larger dense and compactness (i.e., LCZ1~3) imply the stronger CUHII and SUHII at nighttime, especially for LCZ1 (2.7°C in the MS climate zone). The cities with a large proportion of impervious built-up and low-rise buildings (i.e., LCZ8, LCZ3 and LCZ6) experience a stronger daytime SUHII. Urban dwellers are easily exposed to a serious heat stress condition in the NS climate zone, and LCZ3, LCZ7 and LCZ1 experience a lower heat discomfort at daytime, and the compact building types (i.e., LCZ1~3) correspond to a higher heat stress condition at nighttime.

The responses of UHIs and urban heat stress to HW are also explored. CUHII and SUHII are mostly magnified by HW in the humid regions, however, HW weakens daytime and nighttime CUHII as well as daytime SUHII in the arid regions. At daytime, the impacts of HW on LCZ7 and LCZ3 are more significant, and it reaches 0.9 and 0.8 °C in the NS climate zone, respectively. It is larger for the cities with compact buildings (i.e., LCZ1~3) and LCZ7 at nighttime. For daytime SUHII, the cities with a high proportion of impervious surface and low-rise buildings are significantly magnified by HW (2.9°C for LCZ8, in the NS climate zone). It is more likely to be strengthened for the compact building types (1.5°C for LCZ1 and LCZ2, in the NS climate zone) with respect to nighttime SUHII. The occurrence of HW deteriorates the thermal comfort in relatively arid regions, while urban heat risks are alleviated by the HW in most parts of SS climate zone and south-central of MS climate zone. The HW worsens the heat environment especially for the building types with low-rise buildings and high fractions of impervious surfaces (i.e., LCZ3, LCZ6, LCZ7 and LCZ8) in northern climate zones with a relatively arid condition. In the SS climate zone, the cities with open build types (LCZ4~6) or a high proportion of pervious road (LCZ9~10) get more benefits from heat stress at daytime, and HW reduces the heat risk easier in the cities composed of low-rise buildings at nighttime.

Furthermore, We conduct the SUHII attribution to study various contributions from controlling factors to SUHII and the effects of urban features, local climate as well as HW intensity on these factors. The spatial variations of daytime SUHII are dominated by in the arid northern region and r_a in the humid southern region during a heat wave period. The impact of urban features on r_a

contribution is obviously less than background climates, whereas other factors are more easily affected by intra-urban heterogeneity and local climates play a regulating role. The city with an open arrangement of relatively high buildings (LCZ4~5) makes it convect surface heat to the atmosphere more efficiently, and compact types (LCZ1~3) and LCZ8 have a low rate to evaporate water. At nighttime, r_a significantly weakens SUHII, while SUHII is largely strengthened by in the SS, NS, WT climate zone and by Q_s in the MS and MT climate zone. The height of buildings (e.g., LCZ1, LCZ2, LCZ4) reduces the contributions of r_a to SUHII more easily, whereas the compactness of buildings (i.e., LCZ1~3) is important for other factors. The intensifications of r_a, and Q_{ah} to SUHII gradually increase with HW intensity at daytime, while the losses of Rn and Q_s are negative. At nighttime, the positive contributions of and Q_s increase with HW intensity. The amplitudes of I_{slope} of are easier affected by urban features than local climate, while is opposite for I_{slope} of r_a.

The field observations and numerical simulations must be coordinated to validate the performance of CLM5-LCZs. When the LCZs framework are incorporated into models, continuous and valid measurements are necessary for each LCZ that is relatively deficient for the validation of CLM5-LCZs in this study. Additionally, the accuracy of LCZs map need conduct a scientific and rational verification before applying to the simulations at a large scale, and corresponding parameters must be adjusted to represent the form and material for each LCZ. Moreover, urban parameterization should be improved with consideration of the arrangements of buildings, street plants, urban irrigation and purling, and so on, to integrate urban climate, heat mitigation and city planning and to explore the causes of CUHI or SUHI at great length.

Acknowledgments

This study was supported by National Natural Science Foundation of China (Grant No. 41975006). The CLM5-CESM2 employed in the present study is available through a public GitHub repository (http://github.com/ESCOMP/CESM/), and the required rawdata to create the specific surface datasets to run an offline simulation could be downloaded through a separate Subversion input data repository (https://svn-ccsm-inputdata.cgd.ucar.edu/trunk/inputdata/). Atmospheric forcing data for the regional simulation could be obtained at the China Meteorological Forcing Dataset (doi:10.11888/AtmosphericPhysics.tpe.249369.file). The observational data used to evaluate the modified model is available from a network of automatic weather stations through the Jiangsu Meteorological Bureau.

References

https://www.sciencedirect.com/science/article/pii/S2212095515000152

https://journals.ametsoc.org/view/journals/apme/58/9/jamc-d-19-0073.1.xml

https://rmets.onlinelibrary.wiley.com/doi/abs/10.1002/joc.859

https://www.sciencedirect.com/science/article/pii/S221209551830302X

https://www.sciencedirect.com/science/article/pii/S2212095519300239

https://journals.ametsoc.org/view/journals/bams/96/5/bams-d-14-00122.1.xml

https://doi.org/10.1038/s41561-021-00826-w

https://gmd.copernicus.org/articles/8/151/2015/

https://doi.org/10.1038/ncomms12509

https://doi.org/10.1002/joc.2158https://doi.org/10.1002/joc.2158

https://journals.ametsoc.org/view/journals/apme/57/2/jamc-d-17-0101.1.xml

https://journals.ametsoc.org/view/journals/bams/99/9/bams-d-16-0236.1.xml

https://doi.org/10.1029/2019MS001916https://doi.org/10.1029/2019MS001916

https://doi.org/10.1007/s00382-018-4289-x

https://gmd.copernicus.org/articles/9/1937/2016/

https://science.sciencemag.org/content/sci/319/5864/756.full.pdf

https://doi.org/10.1002/joc.2227https://doi.org/10.1002/joc.2227

https://journals.ametsoc.org/view/journals/apme/49/6/2010jamc2354.1.xml

https://rgs-ibg.onlinelibrary.wiley.com/doi/abs/10.1111/j.1475-4959.2007.232_3.x

https://doi.org/10.1007/s41748-020-00193-3

https://acp.copernicus.org/articles/20/6479/2020/

https://doi.org/10.1038/s41597-020-0369-y

https://doi.org/10.1002/joc.7018https://doi.org/10.1002/joc.7018

https://doi.org/10.1038/s41467-021-22799-5

https://journals.ametsoc.org/view/journals/bams/94/9/bams-d-12-00121.1.xml

https://doi.org/10.1080/00045608.2010.497328

https://www.sciencedirect.com/science/article/pii/S2212095521000146

https://doi.org/10.1029/2018MS001583https://doi.org/10.1029/2018MS001583

https://doi.org/10.1029/2020JD034066https://doi.org/10.1029/2020JD034066

https://journals.ametsoc.org/view/journals/apme/52/9/jamc-d-13-02.1.xml

https://advances.sciencemag.org/content/advances/5/4/eaau4299.full.pdf

https://doi.org/10.1029/2020GL091252https://doi.org/10.1029/2020GL091252

https://doi.org/10.1029/2018GL079679https://doi.org/10.1029/2018GL079679

https://journals.ametsoc.org/view/journals/clim/30/2/jcli-d-16-0269.1.xml

https://doi.org/10.1038/s41586-019-1512-9

https://doi.org/10.1007/s00704-005-0142-3

https://doi.org/10.1146/annurev-environ-012320-083623

https://gmd.copernicus.org/preprints/gmd-2021-300/

https://www.sciencedirect.com/science/article/pii/S2210670722002001

https://doi.org/10.1038/s41561-020-00650-8

https://www.sciencedirect.com/science/article/pii/S2212095520303333

https://doi.org/10.1029/2018JD029796https://doi.org/10.1029/2018JD029796

https://www.sciencedirect.com/science/article/pii/S2212095521001516

https://rmets.onlinelibrary.wiley.com/doi/abs/10.1002/qj.49710845502

https://doi.org/10.1002/joc.2201https://doi.org/10.1002/joc.2201

https://journals.ametsoc.org/view/journals/apme/47/4/2007jamc1598.1.xml

https://journals.ametsoc.org/view/journals/apme/47/4/2007jamc1597.1.xml

https://doi.org/10.1029/2018MS001586https://doi.org/10.1029/2018MS001586

https://doi.org/10.1007/s10584-013-0936-8

https://doi.org/10.1007/s00376-021-1371-9

https://doi.org/10.1038/s41467-021-23634-7

https://doi.org/10.1029/2021GL093603https://doi.org/10.1029/2021GL093603

https://www.sciencedirect.com/science/article/pii/S0021999107000459

https://journals.ametsoc.org/view/journals/bams/93/12/bams-d-11-00019.1.xml

https://doi.org/10.1002/joc.3746https://doi.org/10.1002/joc.3746

http://dx.doi.org/10.1088/1748-9326/aa922a

https://doi.org/10.1029/2020MS002382https://doi.org/10.1029/2020MS002382

https://doi.org/10.1038/nclimate2410

https://doi.org/10.1038/s41558-021-01196-2

https://doi.org/10.1029/2020JD033275https://doi.org/10.1029/2020JD033275

https://doi.org/10.1002/joc.2257https://doi.org/10.1002/joc.2257

https://www.sciencedirect.com/science/article/pii/S004896972104239X

https://doi.org/10.1002/joc.4424https://doi.org/10.1002/joc.4424

https://www.sciencedirect.com/science/article/pii/S2210670721001098

https://www.sciencedirect.com/science/article/pii/S0360132320300196

https://www.sciencedirect.com/science/article/pii/S0360132318302130

https://doi.org/10.1038/nature13462

https://doi.org/10.1038/s41558-020-00958-8

http://dx.doi.org/10.1088/1748-9326/aa9f73

https://journals.ametsoc.org/view/journals/hydr/15/3/jhm-d-13-0129_1.xml

https://doi.org/10.1038/s41467-021-24113-9

https://www.sciencedirect.com/science/article/pii/S1352231021005240

https://doi.org/10.1029/2021JD035002https://doi.org/10.1029/2021JD035002

https://doi.org/10.1002/2015JD023909https://doi.org/10.1002/2015JD023909

Alexander, P. J., Mills, G., & Fealy, R. (2015). Using LCZ data to run an urban energy balance model. *Urban Climate, 13*, 14-37. Ao, X., Wang, L., Zhi, X., Gu, W., Yang, H., & Li, D. (2019). Observed Synergies between Urban Heat Islands and Heat Waves and Their Controlling Factors in Shanghai, China. *Journal Of Applied Meteorology And Climatology, 58*(9), 1955-1972. Arnfield, A. J. (2003). Two decades of urban climate research: a review of turbulence, exchanges of energy and water, and the urban heat island. *23*(1), 1-26. Bai, X., Dawson, R. J., Ürge-Vorsatz, D., Delgado, G. C., Barau, A. S., Dhakal, S., et al. (2018). Six research priorities for cities and climate change. *555*(7694), 23-25. Bechtel, B., Alexander, P. J., Beck, C., Böhner, J., Brousse, O., Ching, J., et al. (2019). Generating WUDAPT Level 0 data – Current status of production and evaluation. *Urban Climate, 27*, 24-45. Bechtel, B., Alexander, P. J., Böhner, J., Ching, J., Conrad, O., Feddema, J., et al. (2015). Mapping Local Climate Zones for a Worldwide Database of the Form and Function of Cities. *ISPRS International Journal of Geo-Information, 4*(1). Bechtel, B., Demuzere, M., Mills, G., Zhan, W., Sismanidis, P., Small, C., & Voogt, J. (2019). SUHI analysis using Local Climate Zones—A comparison of 50 cities. *Urban Climate, 28*, 100451. Best, M. J., & Grimmond, C. S. B. (2015). Key Conclusions of the First International Urban Land Surface Model Comparison Project. *Bulletin of the American Meteorological Society, 96*(5), 805-819. Blackport, R., Fyfe, J. C., & Screen, J. A. (2021). Decreasing subseasonal temperature variability in the northern extratropics attributed to human influence. *Nature Geoscience, 14*(10), 719-723. Buzan, J. R., Oleson, K., & Huber, M. (2015). Implementation and comparison of a suite of heat stress metrics within the Community Land Model version 4.5. *Geosci. Model Dev., 8*(2), 151-170. Cao, C., Lee, X., Liu, S., Schultz, N., Xiao, W., Zhang, M., & Zhao, L. (2016). Urban heat islands in China enhanced by haze pollution. *Nature communications, 7*(1), 12509. Chen, F., Kusaka, H., Bornstein, R., Ching, J., Grimmond, C. S. B., Grossman-Clarke, S., et al.

(2011). The integrated WRF/urban modelling system: development, evaluation, and applications to urban environmental problems. *International Journal of Climatology, 31*(2), 273-288. . Chen, Y., & Zhang, N. (2018). Urban Heat Island Mitigation Effectiveness under Extreme Heat Conditions in the Suzhou–Wuxi–Changzhou Metropolitan Area, China. *Journal Of Applied Meteorology And Climatology, 57*(2), 235-253. Ching, J., Mills, G., Bechtel, B., See, L., Feddema, J., Wang, X., et al. (2018). WUDAPT: An Urban Weather, Climate, and Environmental Modeling Infrastructure for the Anthropocene. *Bulletin of the American Meteorological Society, 99*(9), 1907-1924. Danabasoglu, G., Lamarque, J. F., Bacmeister, J., Bailey, D. A., DuVivier, A. K., Edwards, J., et al. (2020). The Community Earth System Model Version 2 (CESM2). *Journal of Advances in Modeling Earth Systems, 12*(2), e2019MS001916. . Daniel, M., Lemonsu, A., Déqué, M., Somot, S., Alias, A., & Masson, V. (2019). Benefits of explicit urban parameterization in regional climate modeling to study climate and city interactions. *Climate Dynamics, 52*(5), 2745-2764. Eyring, V., Bony, S., Meehl, G. A., Senior, C. A., Stevens, B., Stouffer, R. J., & Taylor, K. E. (2016). Overview of the Coupled Model Intercomparison Project Phase 6 (CMIP6) experimental design and organization. *Geosci. Model Dev., 9*(5), 1937-1958. Grimm, N. B., Faeth, S. H., Golubiewski, N. E., Redman, C. L., Wu, J., Bai, X., & Briggs, J. M. (2008). Global Change and the Ecology of Cities. *319*(5864), 756-760. Grimmond, C. S. B., Blackett, M., Best, M. J., Baik, J. J., Belcher, S. E., Beringer, J., et al. (2011). Initial results from Phase 2 of the international urban energy balance model comparison. *International Journal of Climatology, 31*(2), 244-272. . Grimmond, C. S. B., Blackett, M., Best, M. J., Barlow, J., Baik, J. J., Belcher, S. E., et al. (2010). The International Urban Energy Balance Models Comparison Project: First Results from Phase 1. *Journal Of Applied Meteorology And Climatology, 49*(6), 1268-1292. Grimmond, S. (2007). Urbanization and global environmental change: local effects of urban warming. *173*(1), 83-88. Hamdi, R., Kusaka, H., Doan, Q.-V., Cai, P., He, H., Luo, G., et al. (2020). The State-of-the-Art of Urban Climate Change Modeling and Observations. *Earth Systems and Environment, 4*(4), 631-646. Han, W., Li, Z., Wu, F., Zhang, Y., Guo, J., Su, T., et al. (2020). The mechanisms and seasonal differences of the impact of aerosols on daytime surface urban heat island effect. *Atmos. Chem. Phys., 20*(11), 6479-6493. He, J., Yang, K., Tang, W., Lu, H., Qin, J., Chen, Y., & Li, X. (2020). The first high-resolution meteorological forcing dataset for land process studies over China. *Scientific Data, 7*(1), 25. Hertwig, D., Ng, M., Grimmond, S., Vidale, P. L., & McGuire, P. C. (2021). High-resolution global climate simulations: Representation of cities. *International Journal of Climatology, 41*(5), 3266-3285. . Hsu, A., Sheriff, G., Chakraborty, T., & Manya, D. (2021). Disproportionate exposure to urban heat island intensity across major US cities. *Nature communications, 12*(1), 2721. Hurrell, J. W., Holland, M. M., Gent, P. R., Ghan, S., Kay, J. E., Kushner, P. J., et al. (2013). The Community Earth System Model: A Framework for Collaborative Research. *Bulletin of the American Meteorological Society, 94*(9), 1339-1360. Jackson, T. L., Feddema, J. J., Oleson, K. W., Bonan, G. B., & Bauer, J. T. (2010). Parameterization

of Urban Characteristics for Global Climate Modeling. *Annals of the Association of American Geographers, 100*(4), 848-865. Kotharkar, R., Ghosh, A., & Kotharkar, V. (2021). Estimating summertime heat stress in a tropical Indian city using Local Climate Zone (LCZ) framework. *Urban Climate, 36*, 100784. Lawrence, D. M., Fisher, R. A., Koven, C. D., Oleson, K. W., Swenson, S. C., Bonan, G., et al. (2019). The Community Land Model Version 5: Description of New Features, Benchmarking, and Impact of Forcing Uncertainty. *Journal of Advances in Modeling Earth Systems, 11*(12), 4245-4287. . Li, C., & Zhang, N. (2021). Analysis of the Daytime Urban Heat Island Mechanism in East China. *Journal of Geophysical Research: Atmospheres, 126*(12), e2020JD034066. . Li, D., & Bou-Zeid, E. (2013). Synergistic Interactions between Urban Heat Islands and Heat Waves: The Impact in Cities Is Larger than the Sum of Its Parts. *Journal Of Applied Meteorology And Climatology, 52*(9), 2051-2064. Li, D., Liao, W., Rigden, A. J., Liu, X., Wang, D., Malyshev, S., & Shevliakova, E. (2019). Urban heat island: Aerodynamics or imperviousness? *, 5*(4), eaau4299. Liao, W., Li, D., Malyshev, S., Shevliakova, E., Zhang, H., & Liu, X. (2021). Amplified Increases of Compound Hot Extremes Over Urban Land in China. *Geophysical Research Letters, 48*(6), e2020GL091252. . Liao, W., Liu, X., Li, D., Luo, M., Wang, D., Wang, S., et al. (2018). Stronger Contributions of Urbanization to Heat Wave Trends in Wet Climates. *Geophysical Research Letters, 45*(20), 11,310-311,317. . Luo, M., & Lau, N.-C. (2017). Heat Waves in Southern China: Synoptic Behavior, Long-Term Change, and Urbanization Effects. *Journal of Climate, 30*(2), 703-720. Manoli, G., Fatichi, S., Schläpfer, M., Yu, K., Crowther, T. W., Meili, N., et al. (2019). Magnitude of urban heat islands largely explained by climate and population. *Nature, 573*(7772), 55-60. Masson, V. (2006). Urban surface modeling and the meso-scale impact of cities. *Theoretical and Applied Climatology, 84*(1), 35-45. Masson, V., Lemonsu, A., Hidalgo, J., & Voogt, J. (2020). Urban Climates and Climate Change. *Annual Review of Environment and Resources, 45*(1), 411-444. Meier, R., Davin, E. L., Bonan, G. B., Lawrence, D. M., Hu, X., Duveiller, G., et al. (2021). Impacts of a Revised Surface Roughness Parameterization in the Community Land Model 5.1. *Geosci. Model Dev. Discuss., 2021*, 1-44. Miao, S., Zhan, W., Lai, J., Li, L., Du, H., Wang, C., et al. (2022). Heat wave-induced augmentation of surface urban heat islands strongly regulated by rural background. *Sustainable Cities and Society, 82*, 103874. Mishra, V., Ambika, A. K., Asoka, A., Aadhar, S., Buzan, J., Kumar, R., & Huber, M. (2020). Moist heat stress extremes in India enhanced by irrigation. *Nature Geoscience, 13*(11), 722-728. Mughal, M. O., Li, X.-X., & Norford, L. K. (2020). Urban heat island mitigation in Singapore: Evaluation using WRF/multilayer urban canopy model and local climate zones. *Urban Climate, 34*, 100714. Mughal, M. O., Li, X.-X., Yin, T., Martilli, A., Brousse, O., Dissegna, M. A., & Norford, L. K. (2019). High-Resolution, Multilayer Modeling of Singapore's Urban Climate Incorporating Local Climate Zones. *Journal of Geophysical Research: Atmospheres, 124*(14), 7764-7785. . Núñez-Peiró, M., Sánchez-Guevara Sánchez, C., & Neila González, F. J. (2021). Hourly evolution of intra-urban temperature variability across the local climate zones. The case of Madrid. *Urban Climate, 39*, 100921. Oke, T. R. (1982).

The energetic basis of the urban heat island. *108*(455), 1-24. Oleson, K. W., Bonan, G. B., Feddema, J., & Jackson, T. (2011). An examination of urban heat island characteristics in a global climate model. *International Journal of Climatology, 31*(12), 1848-1865. . Oleson, K. W., Bonan, G. B., Feddema, J., & Vertenstein, M. (2008). An Urban Parameterization for a Global Climate Model. Part II: Sensitivity to Input Parameters and the Simulated Urban Heat Island in Offline Simulations. *Journal Of Applied Meteorology And Climatology, 47*(4), 1061-1076. Oleson, K. W., Bonan, G. B., Feddema, J., Vertenstein, M., & Grimmond, C. S. B. (2008). An Urban Parameterization for a Global Climate Model. Part I: Formulation and Evaluation for Two Cities. *Journal Of Applied Meteorology And Climatology, 47*(4), 1038-1060. Oleson, K. W., & Feddema, J. (2020). Parameterization and Surface Data Improvements and New Capabilities for the Community Land Model Urban (CLMU). *Journal of Advances in Modeling Earth Systems, 12*(2), e2018MS001586. . Oleson, K. W., Monaghan, A., Wilhelmi, O., Barlage, M., Brunsell, N., Feddema, J., et al. (2015). Interactions between urbanization, heat stress, and climate change. *Climatic Change, 129*(3), 525-541. Qian, Y., Chakraborty, T. C., Li, J., Li, D., He, C., Sarangi, C., et al. (2022). Urbanization Impact on Regional Climate and Extreme Weather: Current Understanding, Uncertainties, and Future Research Directions. *Advances in Atmospheric Sciences.* Rothfusz, L. P. (1990). *The heat index equation (or, more than you ever wanted to know about heat index).* (Technical Attachment, SR/SSD 90-23). Fort Worth, Texas: National Oceanic and Atmospheric Administration, National Weather Service, Office of Meteorology.Sen, S., & Khazanovich, L. (2021). Limited application of reflective surfaces can mitigate urban heat pollution. *Nature communications, 12*(1), 3491. Shi, Z., Xu, X., & Jia, G. (2021). Urbanization Magnified Nighttime Heat Waves in China. *Geophysical Research Letters, 48*(15), e2021GL093603. . Skamarock, W. C., & Klemp, J. B. (2008). A time-split nonhydrostatic atmospheric model for weather research and forecasting applications. *Journal of Computational Physics, 227*(7), 3465-3485. Stewart, I. D., & Oke, T. R. (2012). Local Climate Zones for Urban Temperature Studies. *Bulletin of the American Meteorological Society, 93*(12), 1879-1900. Stewart, I. D., Oke, T. R., & Krayenhoff, E. S. (2014). Evaluation of the 'local climate zone' scheme using temperature observations and model simulations. *International Journal of Climatology, 34*(4), 1062-1080. . Sun, T., Kotthaus, S., Li, D., Ward, H. C., Gao, Z., Ni, G.-H., & Grimmond, C. S. B. (2017). Attribution and mitigation of heat wave-induced urban heat storage change. *Environmental Research Letters, 12*(11), 114007. Sun, Y., Zhang, N., Miao, S., Kong, F., Zhang, Y., & Li, N. (2021). Urban Morphological Parameters of the Main Cities in China and Their Application in the WRF Model. *Journal of Advances in Modeling Earth Systems, 13*(8), e2020MS002382. . Sun, Y., Zhang, X., Zwiers, F. W., Song, L., Wan, H., Hu, T., et al. (2014). Rapid increase in the risk of extreme summer heat in Eastern China. *Nature Climate Change, 4*(12), 1082-1085. Wang, J., Chen, Y., Liao, W., He, G., Tett, S. F. B., Yan, Z., et al. (2021). Anthropogenic emissions and urbanization increase risk of compound hot extremes in cities. *Nature Climate Change, 11*(12), 1084-1089. Wang, X., Liu, H., Miao, S., Wu, Q., Zhang, N.,

& Qiao, F. (2020). Effectiveness of Urban Hydrological Processes in Mitigating Urban Heat Island and Human Thermal Stress During a Heat Wave Event in Nanjing, China. *Journal of Geophysical Research: Atmospheres, 125*(24), e2020JD033275. . Willett, K. M., & Sherwood, S. (2012). Exceedance of heat index thresholds for 15 regions under a warming climate using the wet-bulb globe temperature. *International Journal of Climatology, 32*(2), 161-177. . Wu, S., Wang, P., Tong, X., Tian, H., Zhao, Y., & Luo, M. (2021). Urbanization-driven increases in summertime compound heat extremes across China. *Science of The Total Environment, 799*, 149166. Xia, J., Tu, K., Yan, Z., & Qi, Y. (2016). The super-heat wave in eastern China during July–August 2013: a perspective of climate change. *International Journal of Climatology, 36*(3), 1291-1298. . Yang, J., Ren, J., Sun, D., Xiao, X., Xia, J., Jin, C., & Li, X. (2021). Understanding land surface temperature impact factors based on local climate zones. *Sustainable Cities and Society, 69*, 102818. Yang, X., Peng, L. L. H., Chen, Y., Yao, L., & Wang, Q. (2020). Air humidity characteristics of local climate zones: A three-year observational study in Nanjing. *Building and Environment, 171*, 106661. Yang, X., Yao, L., Jin, T., Peng, L. L. H., Jiang, Z., Hu, Z., & Ye, Y. (2018). Assessing the thermal behavior of different local climate zones in the Nanjing metropolis, China. *Building and Environment, 137*, 171-184. Zhao, L., Lee, X., Smith, R. B., & Oleson, K. (2014). Strong contributions of local background climate to urban heat islands. *Nature, 511*(7508), 216-219. Zhao, L., Oleson, K., Bou-Zeid, E., Krayenhoff, E. S., Bray, A., Zhu, Q., et al. (2021). Global multi-model projections of local urban climates. *Nature Climate Change, 11*(2), 152-157. Zhao, L., Oppenheimer, M., Zhu, Q., Baldwin, J. W., Ebi, K. L., Bou-Zeid, E., et al. (2018). Interactions between urban heat islands and heat waves. *Environmental Research Letters, 13*(3), 034003. Zhao, W., Zhang, N., Sun, J., & Zou, J. (2014). Evaluation and Parameter-Sensitivity Study of a Single-Layer Urban Canopy Model (SLUCM) with Measurements in Nanjing, China. *Journal of Hydrometeorology, 15*(3), 1078-1090. Zheng, Z., Zhao, L., & Oleson, K. W. (2021). Large model structural uncertainty in global projections of urban heat waves. *Nature communications, 12*(1), 3736. Zhong, T., Zhang, N., & Lv, M. (2021). A numerical study of the urban green roof and cool roof strategies' effects on boundary layer meteorology and ozone air quality in a megacity. *Atmospheric Environment, 264*, 118702. Zonato, A., Martilli, A., Gutierrez, E., Chen, F., He, C., Barlage, M., et al. (2021). Exploring the Effects of Rooftop Mitigation Strategies on Urban Temperatures and Energy Consumption. *Journal of Geophysical Research: Atmospheres, 126*(21), e2021JD035002. . Zou, J., Liu, G., Sun, J., Zhang, H., & Yuan, R. (2015). The momentum flux-gradient relations derived from field measurements in the urban roughness sublayer in three cities in China. *Journal of Geophysical Research: Atmospheres, 120*(20), 10,797-710,809. .